INSTITUTE FOR MICROELECTRONICS

TU WIEN

M A S T E R T H E S I S

Density Functional Theory (DFT) Investigation of Novel Materials for Applications in Sensing

submitted by

Anna Benzer

presented for the degree of

Diplom-Ingenieurin (Dipl.-Ing.)

in

Computational Science and Engineering

supervised by

Associate Prof. Dr.techn. Lado Filipovic

Dipl.-Ing. Dominic Waldhör

at the

Institute for Microelectronics

Vienna, on 5. Oktober 2023

Abstract

Density Functional Theory (DFT) is a well-established method for investigating and modeling the electronic properties of many-body systems. In this thesis, DFT is employed to analyze various possible structures of Metal-Organic Frameworks (MOFs) based on nickel ions and terephthalic acid linkers. Additionally, it is used to model the effect of strain on the band gap of a molybdenum disulfide (MoS_2) monolayer by applying a biaxial strain in the range of –0.5 % to 0.5 %. The resulting band structures are used to determine the effective masses of electrons at the conduction band minima, which provide insights into the influence of strain on intrinsic carrier transport using an Ensemble Monte Carlo approach. Furthermore, the results obtained with different pseudopotentials and exchange-correlation functionals are compared.

Structure optimization calculations for the MOFs systematically showed that compared to the initial structures the complex bonds of the Ni ions were predicted to be tighter and the repulsive forces between the organic linkers to be stronger. This indicates that different types of interactions, especially long-range interactions have not been accounted for accurately. The overall approach proved to be impractical and therefore unsuitable for further explorations.

In the case of MoS_2, it is demonstrated that across all DFT variants, a decrease of mobility for compressive strain is consistently predicted. This can be attributed to the fact that strain induces changes in the conductive band of monolayer MoS_2 in such a way that narrows the gap between two conduction band minima. The smaller energy difference between the conduction band minima induces higher scattering between these two bands, reducing the overall charge carrier mobility. Conversely, tensile strain consistently led to enhanced mobility.

Kurzfassung

Dichtefunktionaltheorie (DFT) ist eine etablierte Methode zur Untersuchung und Modellierung der elektronischen Eigenschaften von Mehrteilchensystemen. In dieser Arbeit wird DFT verwendet, um verschiedene mögliche Strukturen von Metallorganischen Gerüstverbindungen (englisch Metal-Organic Frameworks, MOFs) auf der Basis von Nickelionen und Terephthalsäure-Verbindungselementen zu analysieren. Zusätzlich wird DFT verwendet, um den Effekt von Deformation auf die Bandlücke einer einzelnen Lage Molybdändisulfid (MoS_2) zu modellieren, indem eine Deformation im Bereich von -0,5 % bis 0,5 % angewendet wird. Die resultierenden Bandstrukturen werden verwendet, um die effektiven Massen der Elektronen am Minimum des Leitungsbandes zu bestimmen, was Einblicke in den Einfluss der Deformation auf den intrinsischen Ladungstransport unter Verwendung eines Ensemble-Monte-Carlo-Ansatzes bietet. Darüber hinaus werden die Ergebnisse, die mit verschiedenen Pseudopotentialen und Austausch-Korrelationsfunktionen erhalten wurden, verglichen.

Berechnungen zur Strukturoptimierung der MOFs zeigten systematisch, dass im Vergleich zu den Ausgangsstrukturen die koordinativen Bindungen der Ni-Ionen enger und die abstoßenden Kräfte zwischen den organischen Verbindungselementen als stärker vorhergesagt wurden. Dies deutet darauf hin, dass bestimmte Arten von Wechselwirkungen, insbesondere Wechselwirkungen auf lange Reichweite, nicht genau berücksichtigt wurden. Der gesamte Berechnungsansatz erwies sich als unpraktisch und daher ungeeignet für weitere Untersuchungen.

Im Fall von MoS_2 wird gezeigt, dass über alle DFT-Varianten hinweg konsistent eine Abnahme der Beweglichkeit bei kompressiver Dehnung vorhergesagt wird. Dies kann auf höhere Streuungsraten aufgrund kleinerer Energieunterschiede zwischen den Minima des Leitungsbandes zurückgeführt werden. Im Gegensatz dazu führte eine einheitliche Zugdehnung stets zu einer erhöhten Ladungsträgerbeweglichkeit.

Acknowledgement

Eidesstattliche Erklärung

Ich erkläre an Eides statt, dass ich die vorliegende Diplomarbeit selbstständig und ohne fremde Hilfe verfasst, andere als die angegebenen Quellen und Hilfsmittel nicht benutzt bzw. die wörtlich oder sinngemäß entnommenen Stellen als solche kenntlich gemacht habe.

Wien, am 5. Oktober 2023

Anna Benzer

Contents

1 Introduction

In the modern world, sensors are omnipresent. Whether the goal is the detection of temperature, moisture, pressure, applied strain, or the presence of a specific kind of chemical agent, the applied sensors, like all microelectronic devices, aim to be smaller, more efficient, and cheaper. This necessitates exploring new materials. In this thesis, two different classes of materials are studied and discussed.

The first one is represented by a compound consisting of nickel ions and terephthalic acid linkers, exemplifying the very versatile group of Metal-Organic Frameworks (MOFs). This class of materials consists of highly ordered crystalline coordination polymers with high, designable porosity and large surface areas. These characteristics result in a high density of active sites that can, for example, be utilized in catalytic activity. Furthermore, the application of MOFs in various sensing scenarios has been demonstrated, including the detection of heavy metals, organic pollutants, and gases [1].

The second class uses the highly investigated two-dimensional (2D) material molybdenum disulfide (MoS_2) to showcase 2D transition metal dichalcogenides (TMDs). While 2D materials have demonstrated great potential in various applications, including sensing, their inherent thinness renders them susceptible to environmental factors, particularly their substrate. To limit these influences suspended 2D materials are researched. Their thinness, high conductivity, and strength have already been shown to be beneficial to their application as thermal, optical, pressure, bio, and chemical sensors [2]. Suspended 2D materials also show mechanical characteristics which make them interesting for strain measurements as the influence of substrate-induced strain is minimized. In this thesis, the influence of strain on a suspended MoS_2 monolayer is investigated theoretically.

With growing computational resources, Density Functional Theory (DFT) has established itself as a central means to investigate the electronic structure of many-body systems in condensed matter physics, material sciences, and many other fields. It enables the exploration of hypothetical materials which have not been synthesized yet. Additionally, it serves as a valuable complement to experiments by providing insights into underlying mechanisms. Moreover, DFT makes the efficient screening of promising structures possible, helping to identify candidates worthy of further exploration.

1.1 Aim of Thesis

The aim of this thesis is to apply Density Functional Theory (DFT) together with the Quantum ESPRESSO (QE) open-source software and the CP2K software package to investigate the potential of the two materials for different sensing applications, while also investigating the limitations of these atomistic methods in predicting certain material properties. Different MOF structures are investigated for their optimized geometry and the electronic structure of the MoS_2 monolayer under strain was calculated in order to gain insights into its impact on the carrier mobility. Furthermore, different DFT setups, or "flavors" were used, employing different exchange-correlation functionals and pseudopotentials in order to investigate how the initial choices made for the calculation method influence the results of the *ab initio* calculation. In summary, the principal goal was to explore the possibilities and predictive capabilities of DFT in relation to potential sensor materials, while also assessing computational and methodological limitations.

1.2 Outline of Thesis

This thesis is structured as follows: The Theory section begins with a comprehensive discussion of both materials, Metal-Organic Frameworks (MOFs) and monolayer MoS_2, focusing on their potential applications as future sensing solutions. Additionally, a short overview of Density Functional Theory (DFT) is provided. The Theory section also includes a description of the Ensemble Monte Carlo (EMC) codes which are employed, elaborating on their internal band representation and detailing the calculation of the carrier mobility. In the subsequent Implementation section, the applied computational methods will be described, followed by a step-by-step workflow for the mobility calculation, as well as the procedure for extracting effective masses. Finally, in the Results and Discussion section, the findings of this research will be presented, the insights summarized, and the limitations of the methods discussed.

2 Theory

2.1 Materials

2.1.1 Metal-Organic Frameworks

Metal-Organic Frameworks (MOFs) are a class of highly porous materials constructed by organic linkers and metal nodes. The large variety in the choice of linkers and nodes allows for a high tunability of structure, pore size, and functionality. MOFs have been investigated for a wide range of applications such as gas storage [3], separation [4], heterogeneous catalysis [5], and chemical sensing [6].

Structure

MOFs are constructed by joining metal ions or clusters, also referred to as secondary building units (SBU), with organic linkers. By choosing specific organic ligands and using the geometry of the SBUs, the pore size and functionality of the MOFs can theoretically be designed for an intended application. Very small pores are possible, which only accommodate gases like N_2 or CO_2, while larger ones are also possible, which can hold entire proteins [7]. Multiple functional guests, such as metal atoms, metal complexes, dyes, polymers, and small enzymes can be added to these pores, making even more applications possible [8] [9]. Post-synthetic modifications of MOFs allow for additional functional groups. One challenge faced by MOFs is the often poor stability concerning solvents, heat, or mechanical stress. Water, for example, tends to replace the organic linkers, thereby degrading the MOFs [10]. For applications at higher temperatures, heat stability is essential; this mainly depends on the strength of the bond between node and linkers. Although the porosity and the high surface area of the MOFs are its defining favorable features, they are also its weak points when it comes to mechanical stability. This is a critical factor concerning a MOF's suitability for real-world applications, since it depends on how durable it is, especially when subjected to a mechanical load. On another note, there are also considerations of using this susceptibility to pressure for post-synthetic modifications and to control the MOF's functionality [11].

Ab Initio Studies of MOFs

Due to its composition, the simulation of MOFs can be approached from both a molecular or a material angle. When treated as a bulk solid, applying periodic boundary conditions, the electronic structure can be predicted. Approaching the MOF as an individual molecule enables the utilization of a diverse range of less computationally expensive tools to explore

chemical properties, such as reaction transition states. The accuracy of modeling certain properties largely depends on the chosen functional and basis set. To validate the model's performance, it is essential to compare the results with experimental data or higher-level computational calculations. While the choice of functional depends on the specific MOF, hybrid-GGA methods are widely considered the minimum required level of theory to describe the electronic structure of systems where exchange and correlation play a significant role. Additionally, it is possible to introduce correction terms to account for physical phenomena which are insufficiently described with standard density functional theory (DFT) methods. Most common functionals fail to correctly describe van der Waals interactions for which correctional terms may be added [12]. It might also be reasonable to include a Hubbard U correction to account for erroneous self-interaction of electrons. These corrections should be approached with caution, as the introduced empirical factors have the potential to cause overfitting.[13]

Application as a Sensor

As previously discussed, MOFs are highly tunable, include a wide range of materials, can have multiple functional groups, and can be easily modified. Unsurprisingly, the potential of applying MOFs as sensors is as versatile as the material class itself. For example, luminescent MOFs have been successfully employed to detect specific compounds, for example, nitroaromatic explosives [14], and can also serve as temperature sensors [15]. Functionalized MOFs can be used for biosensing [16], as chemiresistive gas sensors [17], and to detect pH [18]. The tunable pore size also allows for size-selective sensors by using the MOF pores for sieving [19].

2.1.2 Molybdenum disulfide (MoS_2)

Molybdenum disulfide (MoS_2) belongs to a group of 2D layered materials called transition metal dichalcogenides (TMDs). These layers are held together by weak Van-der-Waals forces. The fact that individual monolayers are held by weak forces means that methods like micromechanical exfoliation, where sticky tape is used to peel away layers, or liquid phase exfoliation, can be used to generate single layers of MoS_2 [20]. The MoS_2 monolayers show different properties compared to bulk. Notably, the monolayer has a direct band gap of about 1.8 eV compared to the indirect 1 eV band gap of the bulk material [21], which is one of the properties which make the material highly interesting for a range of electronic applications. The graphene-like structure can be seen in the top view of the monolayer, shown in Fig. 2.1, where the molybdenum atoms are gray and the sulfur atoms are yellow.
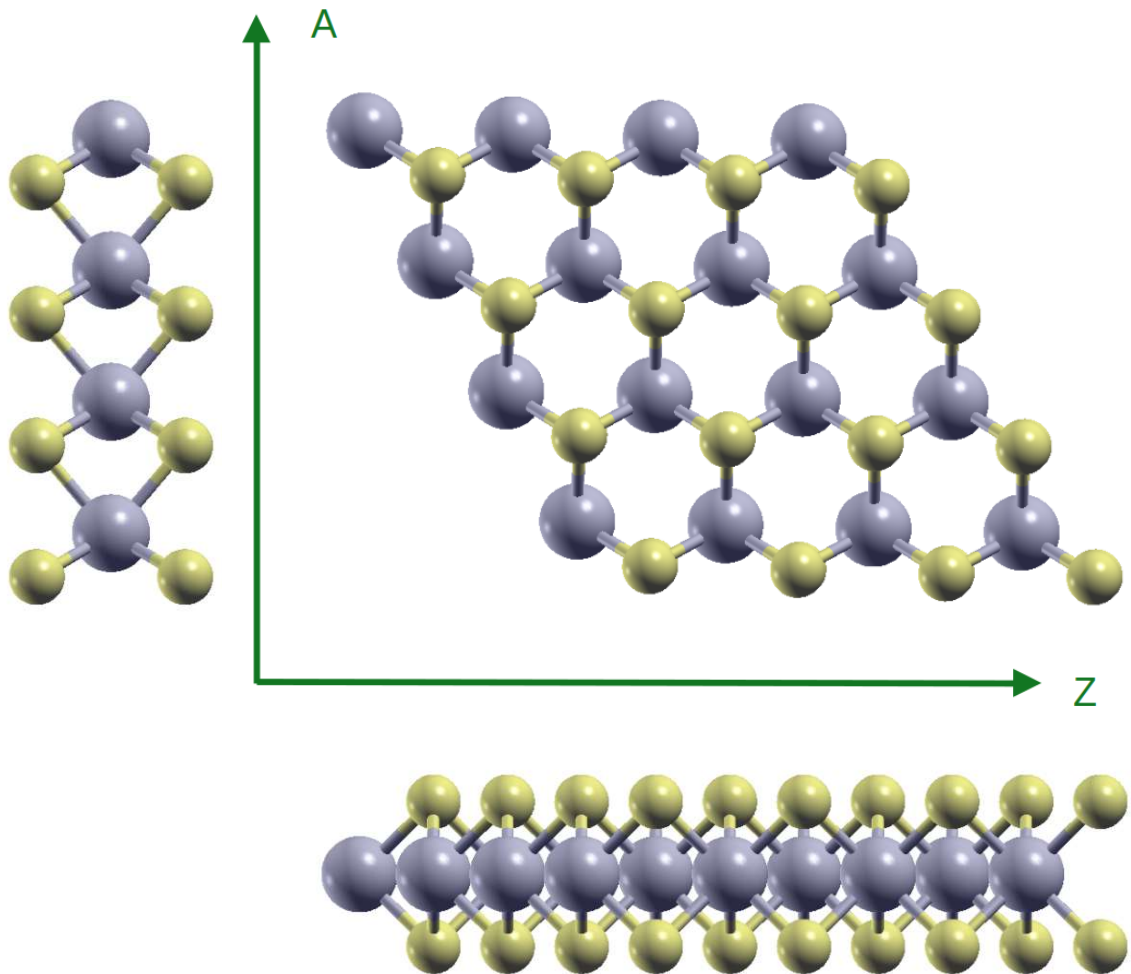
Figure 2.1: Top and side views of monolayer MoS_2 showing its Armchair (A) and Zigzag (Z) directions, visualized with XCrySDen [22].

Application as a Sensor

MoS_2 shows a high specific surface area and great potential for surface modifications which can be used for electrochemical sensing [23]. The fabrication of sensors based on monolayer MoS_2, which changes its conductance based on analyte concentration, has previously been reported [24]. Sensors like this have been realized for various chemical vapors and gases such as CO, CO_2, NO, and NO_2 [25]. Furthermore, the doping of MoS_2 monolayers with various heteroatoms like Au, Pt, Ni [26], and Si [27] to improve adsorption, and therefore detection, of different analyte gases has been theoretically investigated using density functional theory (DFT) and shows promising possibilities for the fabrication of such sensors.

2.2 Density Functional Theory (DFT)

One of the basic concepts of computational quantum mechanics is the solution of the Schrödinger equation (SE) in order to describe the behavior of a system using its wave function Ψ. In its simplest non-relativistic form, the time-independent Schrödinger equation (TISE) is given by

$$\hat{H}\Psi = E\Psi, \tag{2.1}$$

where $\hat{H}$ is the Hamiltonian operator and E is the energy of the system. In other terms, the set of solutions Ψ are eigenstates of the Hamiltonian with corresponding energy eigenvalues E. For systems of one or more atoms, the Hamiltonian consists of multiple terms describing the interactions of electrons (index e) and nuclei (index n). The systems wave function $\Psi(\mathbf{r}, \mathbf{R})$ depends on the positions of all N electrons $(\mathbf{r}_1, \mathbf{r}_2, ..., \mathbf{r}_N)$ and all M nuclei $(\mathbf{R}_1, \mathbf{R}_2, ..., \mathbf{R}_M)$.

The many-body Hamiltonian can be written as

$$\hat{H} = \hat{T}_e + \hat{T}_n + \hat{V}_{en} + \hat{V}_{ee} + \hat{V}_{nn}, \tag{2.2}$$

where the kinetic energy of electrons and nuclei are described by $\hat{T}_e + \hat{T}_n$.

Using atomic units with the reduced Plank constant $\hbar = 1$, the mass of an electron $m_e = 1$, and the electronic charge $e = 1$, the kinetic energy terms are given by

$$\hat{T}_e = -\sum_{i=1}^{N} \frac{1}{2} \nabla_{\mathbf{r}i}^2 \tag{2.3}$$

with the Laplace operator

$$\nabla_{\mathbf{r}_i}^2 = \left(\frac{\partial^2}{\partial \mathbf{r}_{ix}^2} + \frac{\partial^2}{\partial \mathbf{r}_{iy}^2} + \frac{\partial^2}{\partial \mathbf{r}_{iz}^2} \right) \tag{2.4}$$

and analogously for the nuclei

$$\hat{T}_n = -\sum_{i=1}^{M} \frac{1}{2M_i} \nabla_{\mathbf{R}i}^2 \tag{2.5}$$

where M_i is the mass of the nucleus i as a multiple of the electron mass.

The Coulomb interactions of the electrons with the nuclei, the electrons with each other, and the nuclei with each other are accounted for in the terms $\hat{V}_{en} + \hat{V}_{ee} + \hat{V}_{nn}$, respectively [28]. These terms are given by

$$\hat{V}_{en} = -\sum_{i=1}^{N} \sum_{j=1}^{M} \frac{Z_j}{|\mathbf{r}_i - \mathbf{R}_j|} \tag{2.6}$$

$$\hat{V}_{ee} = \frac{1}{2} \sum_{i,j=1}^{N} \frac{1}{|\mathbf{r}_i - \mathbf{r}_j|} \tag{2.7}$$

$$\hat{V}_{nn} = \frac{1}{2} \sum_{i,j=1}^{M} \frac{Z_i Z_j}{|\mathbf{R}_i - \mathbf{R}_j|} \tag{2.8}$$

Unfortunately, this Hamiltonian can only be solved analytically for the hydrogen atom and, despite increasing computational resources, numerical solutions quickly become computationally intractable for all but comparatively small systems.

2.2.1 Born-Oppenheimer Approximation

One of the simplifications which helps make solving the TISE for multiple-atom systems more efficient is the Born-Oppenheimer approximation, which states that the electrons and nuclei can be treated separately, based on the significantly higher mass of the nuclei compared to that of the electrons. Therefore the electrons react much faster to changes in their environment. The nuclei are then treated as fixed in space and the SE is solved for the electrons separately. This implies that the kinetic energy of the nuclei $\hat{T}_n$ can be neglected and the nuclei-nuclei repulsion can be treated as a constant. The electronic TISE can be written as:

$$(\hat{T}_e + \hat{V}_{en} + \hat{V}_{ee})\Psi = E\Psi. \tag{2.9}$$

Here, the nuclear coordinates $\mathbf{R}_i$ are treated as external parameters and the wave function only depends on the electron coordinates $\mathbf{r}_i$.

2.2.2 Kohn-Sham Equations and Exchange-Correlation Functionals

Hohenberg and Kohn state that for an inhomogeneous interacting electron gas in a given potential $v(r)$, there exists a universal functional of the electron density $F[\rho(r)]$ so that the expression

$$E = \int v(r)\rho(r)\mathrm{d}r + F[\rho(r)] \tag{2.10}$$

has as its minimum value the correct ground-state energy. Further if $F[\rho(r)]$ was known and sufficiently simple, the ground-state energy and density in a given external potential could be determined by minimizing the functional of the density function [29].

Based on the theory of Hohenberg and Kohn, a calculation approach was developed by Kohn and Sham [30]. The original many-body problem of interacting electrons and nuclei is mapped to a one-electron reference system with the same density as the real system. With the electron density $\rho(r)$ represented as a sum of single electron densities

$$\rho(r) = \sum_i |\psi_i|^2, \tag{2.11}$$

where ψ_i are single electron wave functions, the Kohn Sham energy functional can be written as

$$E = F[\rho] = T_s[\psi_i] + E_H[\rho] + \int v_{ext}(\mathbf{r})\mathrm{d}^3r + E_{xc}[\rho], \tag{2.12}$$

where $T_s[\psi_i]$ is the kinetic energy and E_H is the Hartree energy, accounting for the electrostatic energy associated with the charge distribution. The Hartree energy, expressed in terms of the electron density is given by

$$E_H = \frac{1}{2} \int \int \frac{\rho(\mathbf{r})\rho(\mathbf{r'})}{|\mathbf{r}-\mathbf{r'}|} \mathrm{d}^3\mathbf{r}\,\mathrm{d}^3\mathbf{r'} \tag{2.13}$$

where v_{ext} is the external potential containing all potentials acting on the electrons, except their interactions with each other, and E_{xc} is the exchange-correlation energy, accounting for all many-body exchange and correlation effects. The exchange-correlation energy is defined such that the total energy is exact. Therefore, if this exchange-correlation term was known exactly, solving the Kohn-Sham equations would allow to calculate the exact ground-state energy and the related density of the many-body electron system. As this is not the case, approximations are necessary, which will be discussed below.

One remaining question is how to determine the ground-state density ρ_0 which minimizes the total energy in Eq. (2.12). The solution is based on the variational principle.

With the condition

$$\int \delta\rho(\mathbf{r})\mathrm{d}\mathbf{r} = 0, \tag{2.14}$$

based on the stationary property of Eq. (2.12), the equation

$$\int \delta\rho(\mathbf{r}) \left\{ \varphi(\mathbf{r}) + \frac{\delta T_s[\rho]}{\delta\rho(\mathbf{r})} + \mu_{xc}(\rho(\mathbf{r})) \right\} \mathrm{d}\mathbf{r} = 0 \tag{2.15}$$

is obtained, where the potential in which the noninteracting electrons move is given by

$$\varphi(\mathbf{r}) = v_{ext}(\mathbf{r}) + \int \frac{\rho(\mathbf{r'})}{|\mathbf{r}-\mathbf{r'}|}\mathrm{d}\mathbf{r'} \tag{2.16}$$

and

$$\mu_{xc}(\rho) = \mathrm{d}(\rho\varepsilon_{xc}(\rho))/\mathbf{d}\rho, \tag{2.17}$$

which gives the exchange-correlation contribution to the chemical potential of a uniform electron gas with density ρ. The density can be determined by solving the one-particle Schrödinger equation

$$\left\{-\frac{1}{2}\nabla^2 + [\varphi(\mathbf{r}) + \mu_{xc}(\mathbf{r})]\right\}\psi_i(\mathbf{r}) = \varepsilon_i\psi(\mathbf{r}) \tag{2.18}$$

These equations have to be solved self-consistently: An ansatz for an initial density is made and used to construct $\varphi(\mathbf{r})$ from Eq. (2.16) and μ_{xc} from Eq. (2.17) which are used to determine a new $\rho(\mathbf{r})$ from Eq. (2.18) and (2.11).

The final energy is then given by [30]

$$E = \sum_1^N \varepsilon_i - \frac{1}{2}\int\int \frac{\rho(\mathbf{r})\rho(\mathbf{r'})}{|\mathbf{r}-\mathbf{r'}|}\mathrm{d}^3\mathbf{r}\,\mathrm{d}^3\mathbf{r'} + \int \rho(\mathbf{r})[\varepsilon_{xc}(\rho(\mathbf{r})) - \mu_{xc}(\rho(\mathbf{r}))]\mathrm{d}\mathbf{r}. \tag{2.19}$$

There are several different approaches for applying these exchange-correlation functionals and only the ones used in this thesis are mentioned below:

Local density approximation (LDA)

Local density approximation (LDA) [30] uses the homogenous electron gas as a model to derive the terms for exchange and correlation which only depend on $\rho(r)$:

$$E_{xc}^{LDA}[\rho] = \int \varepsilon_{xc}(\rho(r))\rho(r)\mathrm{d}^3 r. \tag{2.20}$$

For the exchange energy in volume V the exact analytical expression for the homogenous electron gas can be used:

$$E_x = -\frac{3}{4}\left(\frac{3}{\pi}\right)^{\frac{1}{3}} n^{\frac{4}{3}} V \tag{2.21}$$

For the correlation energy, a function was fitted to data from a quasi-exact Monte-Carlo simulation [31].

Generalized gradient approximations (GGA)

To enhance the accuracy beyond the limitations of LDA, which tends to overbind and struggles with rapidly changing charge densities, the generalized gradient approximation (GGA) was introduced, which includes a dependence on the gradient of the density:

$$E_{xc}^{GGA}[\rho] = \int \varepsilon_{xc}(\rho(r), \nabla\rho(r))\rho(r)\mathrm{d}^3 r \tag{2.22}$$

The most famous example of this type is the Perdew, Burke, and Ernzerhof (PBE) exchange-correlation functional [32]. Another functional used in this thesis is called PBESOL which is specially modified for solids [33].

Hybrid

Hybrid functionals combine Hartree-Fock and density-dependent functionals. They are more computationally expensive, when compared to LDA and GGA, but they show much better results for calculating band gap and excitation energies. [34]

2.2.3 Pseudopotentials

Another approximation, which allows for a faster and more efficient solution of the SE is the use of pseudopotentials. The effects of the tightly bound core electrons and the Coulomb potential of the nucleus are replaced by an effective ionic potential and only the valence electrons are described using pseudo-wave functions. It is possible to generate a pseudopotential in atomic calculations as the core states barely change, depending on the chemical environment of the atom. [34]

A short overview of the types of pseudopotentials used in this thesis is provided below:

Norm-conserving pseudopotentials

For a pseudopotential, it is essential that, even though it is constructed in one specific environment, it can be used to accurately describe the valence properties in different environments like atoms, ions, molecules, or solids. In 1979, Hamann, Schlüter, and Chiang proposed four desirable properties for pseudopotentials to improve their transferability and to ensure accurate results:

- The valence eigenvalues for a chosen reference atomic configuration agree.

- Beyond a chosen cutoff radius r_c the real- and pseudo-wave functions agree.

- Norm conservation: The integrals from 0 to r for r bigger than r_c of the real- and pseudo-charge densities agree. This property guarantees that the electrostatic potential outside r_c is identical for real- and pseudo-charge distributions.

- The first energy derivative of the logarithmic derivatives of the all-electron and pseudo wave functions agrees at r_c, and therefore for all $r \geq r_c$. This ensures scattering properties of the real ion cores are reproduced with minimum error.

In Fig. 2.2 the real- and pseudo-wave functions of Mo are compared for s, p, and d orbitals, it can be seen that beyond r_c real- and pseudo-wave functions agree. Furthermore, the bare-ion pseudopotential can be observed, which is similar and weak for s and p, but has a strong attractive well for d [35].

Ultra soft pseudopotentials

By increasing the cutoff radius and ensuring optimal smoothness of potential and wave function, the basis-set size can be reduced further. The "ultra soft" refers to these larger cutoff radii. To enable this optimal smoothness the norm-conserving constraint is removed [36].

Projector Augmented Wave (PAW)

The projector augmented wave (PAW) potential expresses the valence wave-functions as a sum of smooth functions and core functions. PAW retains the complete set of all-electron core functions along with smoothed valence functions, while maintaining the advantage of pseudopotentials of easy force calculations [34].

2.2.4 Spin Orbit Coupling

Quantum effects which arise when particles are in motion can be better understood by considering their spin and how it interacts with their motion through spin-orbit coupling. A particle's spin is quantized and can only take two discrete values: $\pm\hbar/2$, and when particles are in motion, their spin can influence how they behave in a quantum way. Especially for heavy atoms, the electrons can reach high speeds making it necessary to consider relativistic effects. As spin-orbit coupling is the connection between a particle's spin and its momentum (motion) it is a key factor which brings out quantum relativistic effects in materials. [37]
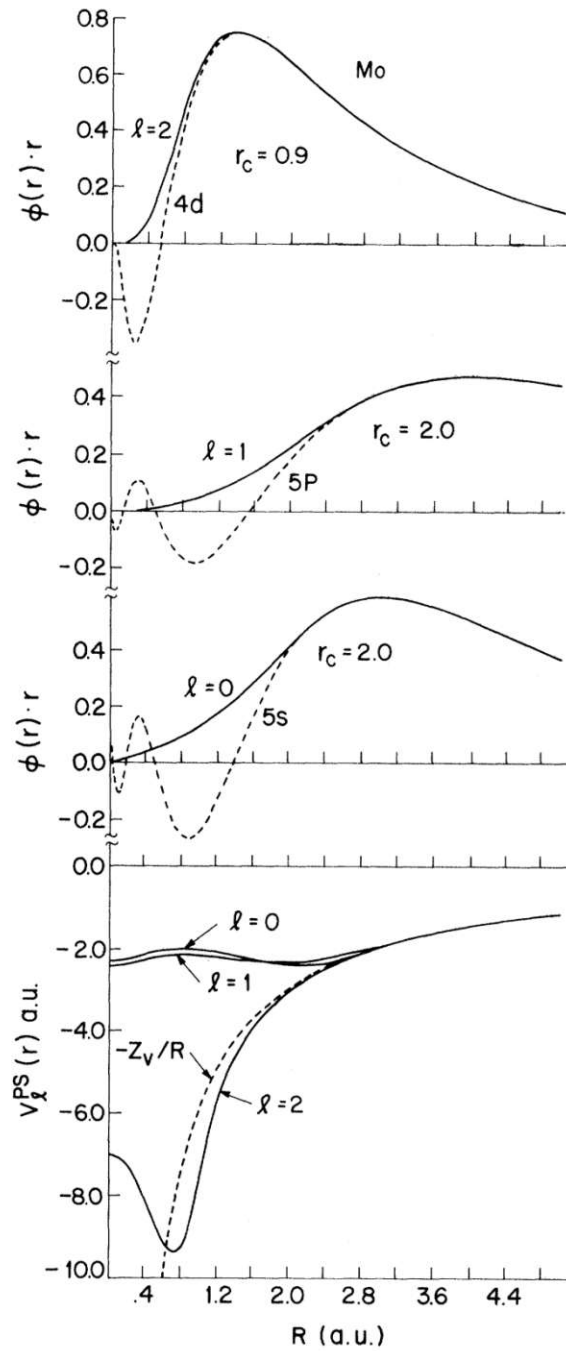
Figure 2.2: Illustration of pseudopotentials for Mo comparison of norm-conserving pseudo-wave functions (solid) and full-core atomic valence wave functions (dashed line). Reprinted figure with permission from [35], Copyright (1971) by the American Physical Society.

11

The magnetic moment of a particle is connected to its total angular momentum $\vec{J}$, which combines the spin angular momentum $\vec{S}$ and the orbit angular momentum $\vec{L}$. When taking relativistic effects into account, those two contributions cannot be separated, and spin-orbit coupling needs to be taken into consideration. In Quantum ESPRESSO [38], [39], a suite of tools for electronic-structure calculations and materials modeling codes used in this thesis, this is implemented using the standard basis of separable atomic functions $R_l(r)Y_{lm}(\theta, \phi)\chi(\sigma)$. Here, the radial function $R_l(r)$ is an eigenfunction of the pseudo-atom; $Y_{lm}(\theta, \phi)$ stands for the spherical harmonics and $\chi(\sigma)$ are spin up/down projectors. When spin-orbit coupling is present, the radial functions $R_{l\pm1/2}(r)$ are taken from fully-relativistic pseudopotential files and averaged to construct $R_l(r)$.

2.3 Ensemble Monte Carlo

To describe how the mobility of the MoS$_2$ monolayer under strain is calculated, some theoretical concepts behind the applied Ensemble Monte Carlo (EMC) code will shortly be elaborated on. This includes the description of the band structure, using an effective mass approximation, the underlying semi-classical transport theory, the scatter mechanisms, and the basics of the EMC codebase.

2.3.1 Effective Mass Approximation

While it is possible to implement a model which includes the full band structure, see Fig. 2.3, this is linked to a significantly higher computational effort. Therefore, the band structure is approximated in the EMC code, focusing on the valence and conduction bands. Charge carrier scattering mechanisms which have a significant influence on the carrier mobility, take place inside and in-between the valleys of the conduction band, meaning that its description is essential. The description of the multiple valleys is done using an effective mass approach, in which the carriers are treated as free particles, but their mass is adjusted to account for the influence of the potential.

For a parabolic dispersion relation $E(\mathbf{k})$, the effective mass m^* can be calculated by its curvature, using

$$m^* = \hbar^2 [\frac{d^2 E(\mathbf{k})}{d\mathbf{k}^2}]^{-1}. \tag{2.23}$$

For a free electron, this would be a perfect parabola, with a constant mass equal to the actual electron mass. This approximation is used to describe the (local) extrema of the bands which ideally have a parabolic shape. In the Ensemble Monte Carlo code, this is performed for the valleys at the Q- and K- points of the MoS$_2$ monolayer.

The MoS$_2$ shows n-type behavior which means electrons are the majority carriers and the conduction band is occupied by electrons. Processes in which electrons transition between different energy bands are not taken into consideration. The electron mobility mainly depends on the conduction band and lower bands including the valence band can be neglected. Under conditions under which the energies of the electrons are low, therefore
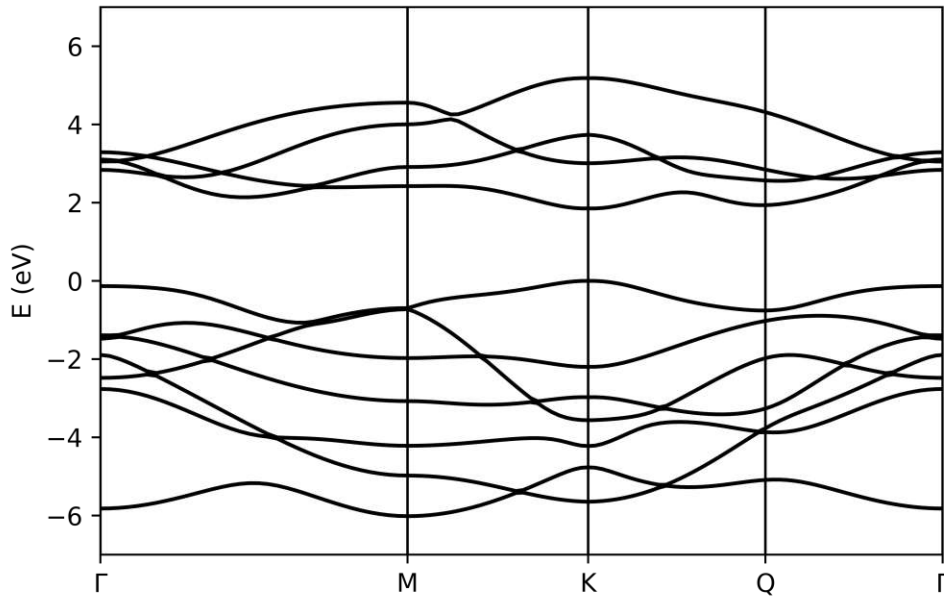
Figure 2.3: Band structure of Monolayer MoS_2.

no elevated temperatures and low electric fields, the electrons are mainly occupying states at the conduction band minima, which are, as can be seen in Fig. 2.4 situated at the Q- and K-points. Therefore most scattering events limiting the mobility can be assumed to occur in and in between these valleys, justifying this approximation.
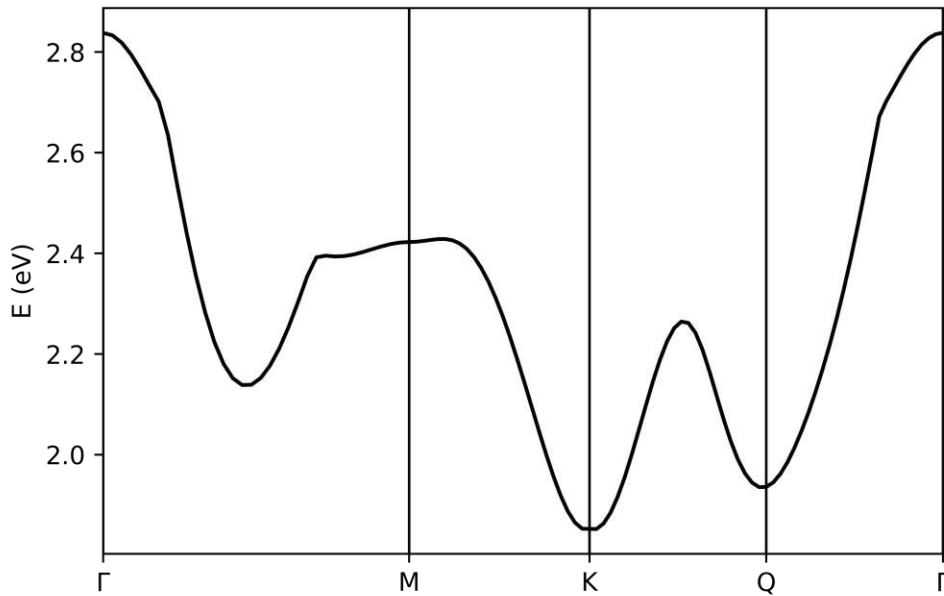
Figure 2.4: Conduction band of Monolayer MoS_2.

The atomistic material simulation is performed in three dimensions, but due to the two-dimensional (2D) nature of the material, the effective mass is only calculated for the two dimensions spanning the monolayer plane. As can be seen in Fig. 2.5, showing the first Brillouin zone of the MoS_2 layer, the valley at the K point (red) is spherical and the valley at the Q point elliptical (blue).
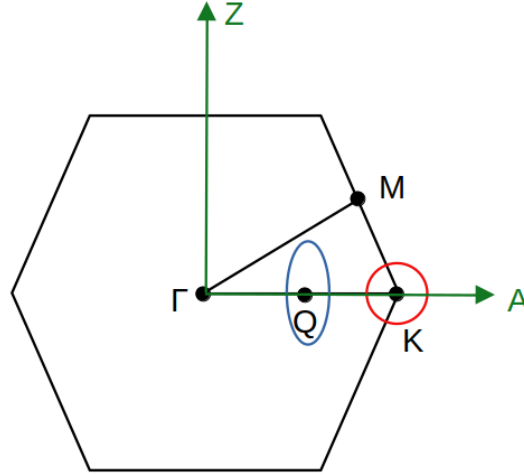

Figure 2.5: Brillouin zone of Monolayer MoS_2 with K valley (red) and Q valley (blue).

Therefore, it is necessary to describe the effective mass at the Q point in terms of a transversal effective mass m_t, the direction of the direct path from Γ to K, and of a longitudinal effective mass m_l which is the direction perpendicular to it. For the Q point (shown in Fig. 2.5), these directions would correspond to the Armchair direction for m_t and the Zigzag direction for m_l. As the valley at the K point is spherical, these two masses should be identical. The relation between energy and wave-vector $\mathbf{k} = (k_l, k_t)$ is given by equation (2.24)

$$E(1 + \alpha E) = \frac{\hbar^2 k_l^2}{2m_l} + \frac{\hbar^2 k_t^2}{2m_t}, \tag{2.24}$$

with α as the non-parabolicity factor (eV^{-1}) [40]. In the Effective Mass Approximation (EMA), initially, a parabolic dispersion relation is assumed for charge carriers. However, real-world electronic band structures often deviate from this ideal parabolic shape, which can reduce the accuracy of the EMA. The non-parabolicity factor is introduced to account for these deviations. Figure 2.6 shows how the curves can be used to approximate the conduction band at the Q and K points.
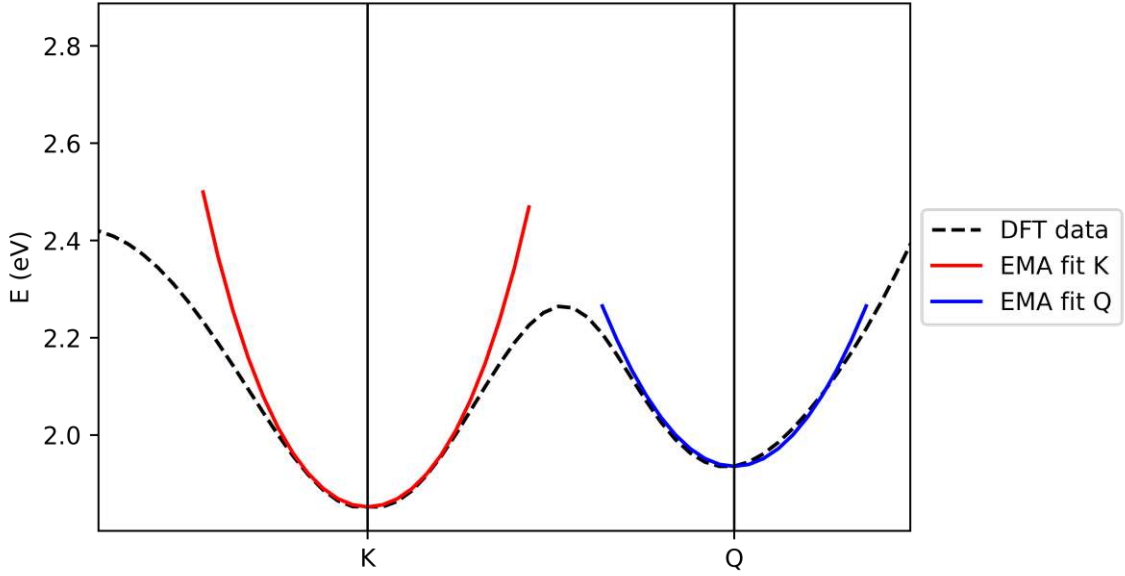
Figure 2.6: Conduction band of Monolayer MoS$_2$ including the dispersion relation curves resulting from the EMA for the K and the Q valley.

2.3.2 Semi-Classical Charge Carrier Transport

The semi-classical method for simulating charge carrier transport is suitable for devices which have feature dimensions much longer than the mean free path between collisions. For silicon, where the electron mean free path is on the order of about 10 nm, this approach can be used and has been applied extensively in the past. The method is typically applied to calculate the transport parameters such as charge carrier mobility and conductivity [41]. At its core, the semi-classical method solves the Boltzmann Transport Equation (BTE), which can be done by Microscopic and Macroscopic approaches, shown in Fig. 2.7.

In order to determine the carrier mobility of the 2D MoS$_2$ film, the Monte Carlo Method, as implemented in the ViennaEMC Semiconductor Device Simulation library [42], was used. In semi-classical transport theory, particles are described by their position $\mathbf{r}$ and their momentum which is described with the wave vector $\mathbf{k}$. The probability of finding a carrier in state $(\mathbf{r}, \mathbf{k})$ is given by a distribution function $f(\mathbf{r}, \mathbf{k}, t)$ and how this distribution function changes, is described by the Boltzmann transport equation (BTE)

$$\frac{\partial f(\mathbf{r}, \mathbf{k}, t)}{\partial t} + \left(\frac{\partial f}{\partial t}\right)_{diff} + \left(\frac{\partial f}{\partial t}\right)_{force} = \left(\frac{\partial f}{\partial t}\right)_{coll}, \tag{2.25}$$

or

$$\frac{\partial f(\mathbf{r}, \mathbf{k}, t)}{\partial t} + \mathrm{v}(k) \cdot \nabla_{\mathbf{r}} f + \frac{\mathbf{F}}{\hbar} \cdot \nabla_{\mathbf{k}} f = \left(\frac{\partial f}{\partial t}\right)_{coll}. \tag{2.26}$$

The first term in equation (2.25) accounts for the time dependence of the distribution function. The diffusion term, denoted by $diff$ describes the spatial variations of the distribution function, and the force term, denoted by $force$ captures the acceleration caused by
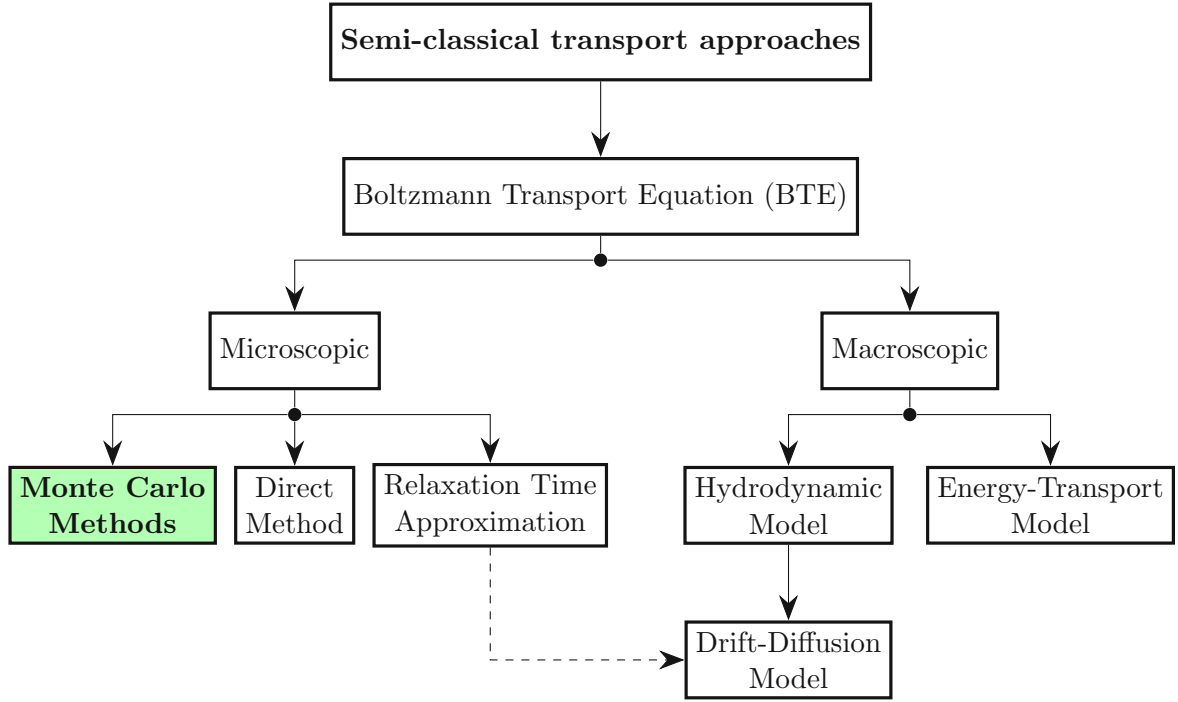
Figure 2.7: Semi-classical approaches for calculating charge carrier transport. The green rectangle depicts the method used in this thesis, mainly Ensemble Monte Carlo, a microscopic approach to solving the BTE.

the Lorentz force. Lastly, the collision term (*coll*) describes how the distribution function changes due to scattering events. This term holds particular significance within the scope of this thesis as it strongly impacts carrier mobility [43]. While the carriers are treated classically and particle-like for the *diff* and *force* terms, the quantum-mechanical effects come into play in the collision term. The collision term can be seen as the sum of the differences of the in- and out-flow of particles in the state $(\mathbf{r}, \mathbf{k})$, which is given by

$$\left(\frac{\partial f}{\partial t}\right)_{coll} = \sum_{\mathbf{k'}} \left(f(\mathbf{r}, \mathbf{k'}, t)[1 - f(\mathbf{r}, \mathbf{k}, t)]\Gamma(\mathbf{k'}, \mathbf{k}) - f(\mathbf{r}, \mathbf{k}, t)[1 - f(\mathbf{r}, \mathbf{k'}, t)]\Gamma(\mathbf{k}, \mathbf{k'})\right).$$
(2.27)

Equation (2.27) essentially describes the change of the distribution function by quantifying how many particles with an initial state $(\mathbf{r}, \mathbf{k'})$ change into the state $(\mathbf{r}, \mathbf{k})$ (in-scattering flow) minus the number of particles of an initial state $(\mathbf{r}, \mathbf{k})$ changing into another state $(\mathbf{r}, \mathbf{k'})$ (out-scattering flow). These changes depend on the probability of the first state being occupied, given by $f(\mathbf{r}, \mathbf{k_{first}}, t)$ the second state being empty $[1 - f(\mathbf{r}, \mathbf{k_{second}}, t)]$, and the total scatter rate for a particle which is to scatter from state $\mathbf{k}$ to $\mathbf{k'}$, given as $\Gamma(\mathbf{k}, \mathbf{k'})$ [44]. The rate $\Gamma(\mathbf{k}, \mathbf{k'})$ can be described by Fermi's golden rule, which comes from perturbation theory. The probability of the second state being empty is essential because, for electrons, which are fermions, the Pauli Exclusion Principle applies, and not two of them can occupy the same quantum state at the same time.

Solving the BTE analytically is complicated and not always possible. For this reason, stochastic Monte Carlo solvers are often applied to approximate the solution numerically and solve for the distribution function $f(\mathbf{r}, \mathbf{k}, t)$, which is derived from the average characteristic quantities of interest, such as carrier energies, densities, currents and the carrier mobility.

2.3.3 Scattering

A scattering event can change a particle's wave vector $\mathbf{k}$ and the energy band to which it is assigned. When these bands are approximated using multiple valleys, the scattering event can also lead to a change of valleys belonging to the same band. As already mentioned, transition rates for a particle from a state $\mathbf{k}$ and a band v to a state $\mathbf{k}$' and a band w can be described by Fermi's Golden rule. The total scatter rate is simply the sum of all the rates for all scatter mechanisms included in the simulation.

There is a multitude of scattering mechanisms for which the occurrence and importance depend on the device/materials under study. An overview of the typical scattering mechanisms occurring in semiconductors is given in Fig. 2.8. In general, the scattering of charge carriers can be caused by stationary defects such as dislocations, neutral and ionized impurities, and dynamic defects in the form of carriers and lattice phonons [45]. In lattice scattering mechanisms, distinctions are made regarding whether an acoustic or optical phonon is involved and whether this causes the particle to stay in the same valley (intravalley scattering) or change into another valley (intervalley scattering). Only the mechanisms used in the EMC simulation of MoS$_2$ within the scope of this thesis will be described here in more detail.

Using effective deformation potentials, the phonon-based scattering can be described, and the rate of acoustic intravalley scattering can be written as

$$\Gamma_{ac}(\mathbf{k}, \mathbf{k'}) = \frac{2\pi k_B T D_{ac}^2}{\rho S \hbar v_s^2} \delta[E(\mathbf{k'}) - E(\mathbf{k})], \quad (2.28)$$

with k_B the Boltzmann constant, T the temperature, D_{ac} the acoustic deformation potential, S the normalized area, ρ the density, and v_s the sound velocity. For the intervalley scattering, which can be assisted by both optical and acoustic phonons, the rate can be calculated as

$$\Gamma_{ac/op}^{v,w}(\mathbf{k}, \mathbf{k'}) = \frac{\pi (D_{ac/op}^{v,w})^2}{\rho S \omega_{ac/op}} [n_{op} + \frac{1}{2} \mp \frac{1}{2}] \delta[E^w(\mathbf{k'}) - E^v(\mathbf{k}) \mp \hbar \omega_{ac/op}(q)], \quad (2.29)$$

with $D_{ac/op}^{v,w}$ as the deformation potential for the transition from valley v to valley w, and n_{op} the phonon occupation number which is determined based on the Bose-Einstein distribution [40]. The phonon energies and the deformation potentials used are obtained from [46].

2.3.4 Ensemble Monte Carlo Method

The Ensemble Monte Carlo (EMC) method is used to numerically approximate non-equilibrium transport for the simulation of semiconductor devices and materials by solving
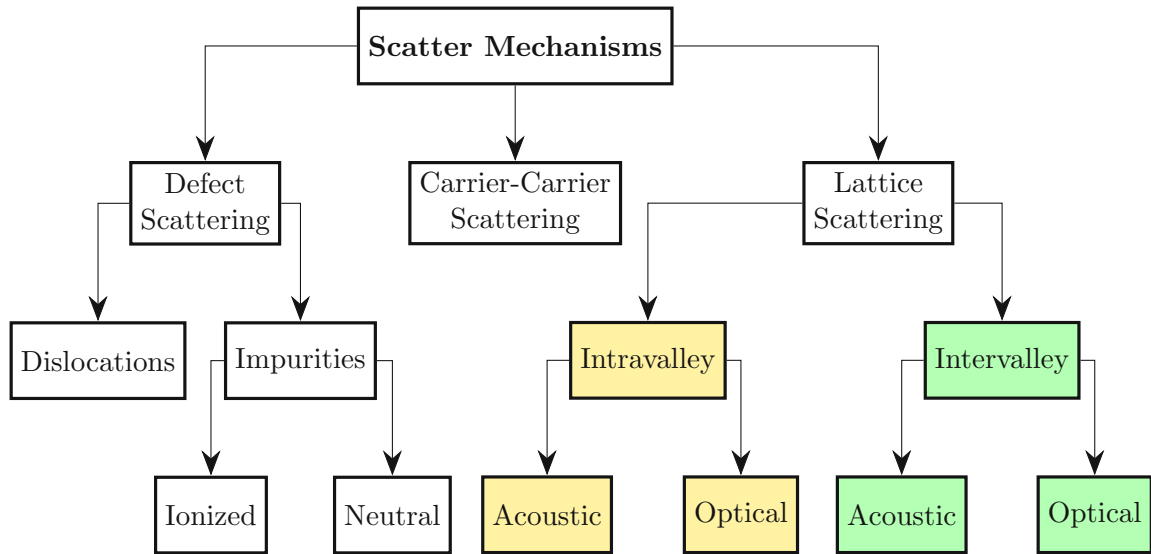
Figure 2.8: Overview on types of scatter mechanisms in semiconductors. For this study, we concentrate on the intervalley scattering between the Q and K valleys, the mechanisms marked in green. Nevertheless, intravalley scatter mechanisms are also included in the ViennaEMC code, identified in yellow.

the BTE. Random numbers are used to determine the motion of sample particles which move simultaneously during small time steps Δt. The trajectories of the particles in phase space are tracked and their mean characteristics are determined between the steps. These characteristics of the resulting random walks fulfill the BTE in the long time limit [44].

The code itself allows for the simulation of devices as well as bulk materials. In the scope of this thesis, the focus will be on the simulation of material properties, and will not concern itself with device simulation directly. For further details on the Ensemble Monte Carlo Framework see the Master Thesis "Development and Application of an Ensemble Monte Carlo Framework" by Laura Gollner [47].

The general workflow of the EMC bulk simulation is depicted in Fig. 2.9 and can described as follows: First, the input parameters have to be defined, which include material characteristics such as the band structure and the applied background field, the particle type, and information about the scatter mechanisms. Additionally, simulation parameters such as the total simulation time and time step Δt need to be set. Subsequently, the simulation is initialized. This includes pre-calculating scatter rates and defining the individual particle energies, positions, and wave vectors. Then, the simulation itself is performed, which includes looping over all time steps of Δt until the total simulation time is reached. The last step is to extract and store the final simulation results [47].
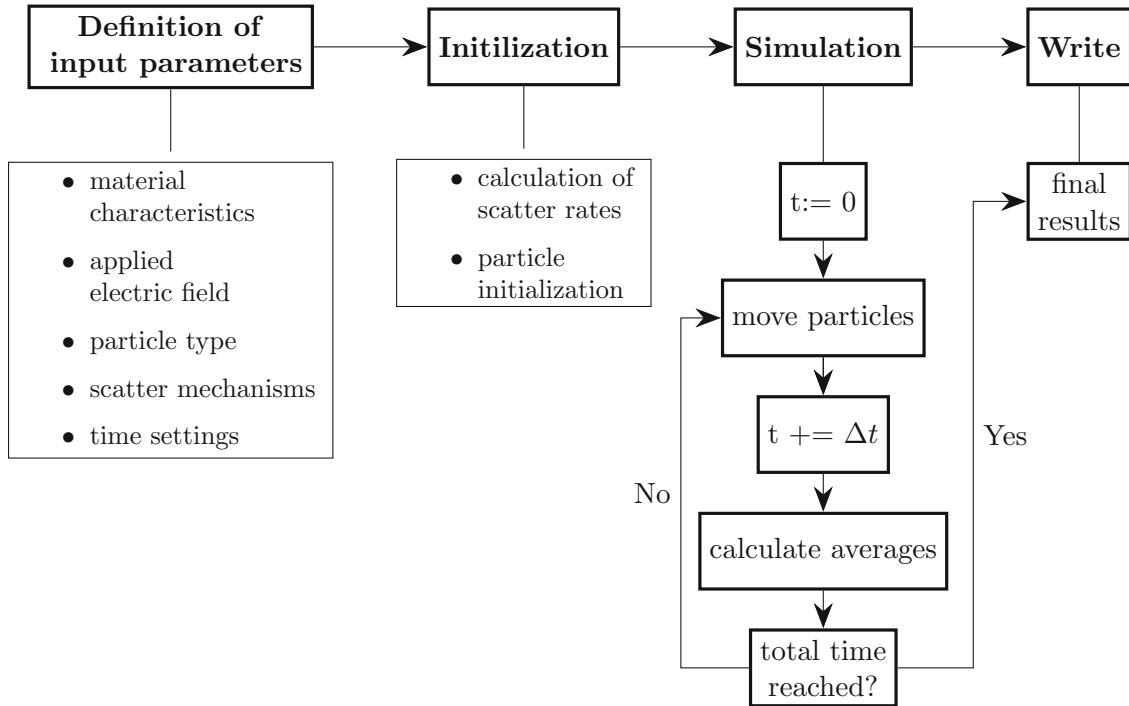
Figure 2.9: Vienna EMC workflow for bulk simulations.

2.3.5 Mobility Calculation

The mobility μ of the charge carriers can be determined using bulk simulations of a material, such as monolayer MoS_2 in this work. In the approach used, μ is calculated based on the diffusion coefficient at zero field via the auto-correlation function. The velocity of each particle is recorded over several time steps and used to derive the auto-correlation. This is then applied to calculate the diffusion coefficient D from which the mobility can be extracted using the Einstein relation

$$D = \frac{\mu k_b T}{q},\tag{2.30}$$

where k_b is the Boltzmann constant and q is the elementary charge [47], [48].

3 Implementation

3.1 Metal-Organic Frameworks

The sample MOF, synthesized using terephthalic acid linkers and nickel ions, was to be investigated for its possible molecular structure, in order to make predictions about its stability, as well as its physical and chemical properties. For this, four different structures with the same basic components were investigated. One, with the molecular formula $Ni_4C_{16}H_{12}O_{13}$, was based on the publication by Zhao et al. [49], where the material was proposed as an electrocatalyst for the oxygen evolution reaction. The three alternative structures come from the materials project MOF Explorer [50] which includes several MOF databases, including the QMOF database [51], [52] from which the alternative structures were taken.

All following illustrations of the MOF structures, presented in Fig. 3.1, were made using the 3D visualization program VESTA [53].

The intention of this study was to investigate these four structures using DFT as implemented in the CP2k code [54]. However, ensuring that the calculations converge proved to be quite difficult after many variations were attempted: different exchange-correlation functionals, changing the number of inner and outer self-consistent field (scf) steps, changing the minimizer used, using supercells, and k-points. Finally, the convergence was still shown to be quite poor and the calculations required long execution times. Additionally, using the PBE functional led to a significant underestimation of the band gap. This incorrectly suggested that the MOFs are conductors and not, as expected, insulators. To circumvent this, the functional was changed to the PBE0 [55] hybrid functional. To improve convergence, the simulated cell was duplicated with the aim of creating, as far as possible, supercells of equal extent in all dimensions.

3.1.1 Cutoff Convergence and Structure Optimization

The method applied within the scope of this thesis to calculate the forces in the CP2K code is called QUICKSTEP. In QUICKSTEP, the representation of certain functions requires the use of an integration grid. More specifically, the method uses a multi-grid approach, allowing smooth Gaussian functions to be mapped on coarser grids and sharper Gaussian functions on finer grids. A sufficiently fine integration grid is essential for accurate and reliable results. This makes it necessary to perform a cutoff convergence for the CUTOFF and REL_CUTOFF parameters. The default four grid levels were used. The CUTOFF keyword defines the plane-wave cutoff in terms of Rydberg (Ry) of the finest level. The

(a) Proposed structure [49] ($Ni_4C_{16}H_{12}O_{12}$).

(b) Alternative structure A ($Ni_2C_{16}H_{24}O_{16}$).

(c) Alternative structure B ($Ni_3C_{16}H_{14}O_{12}$).

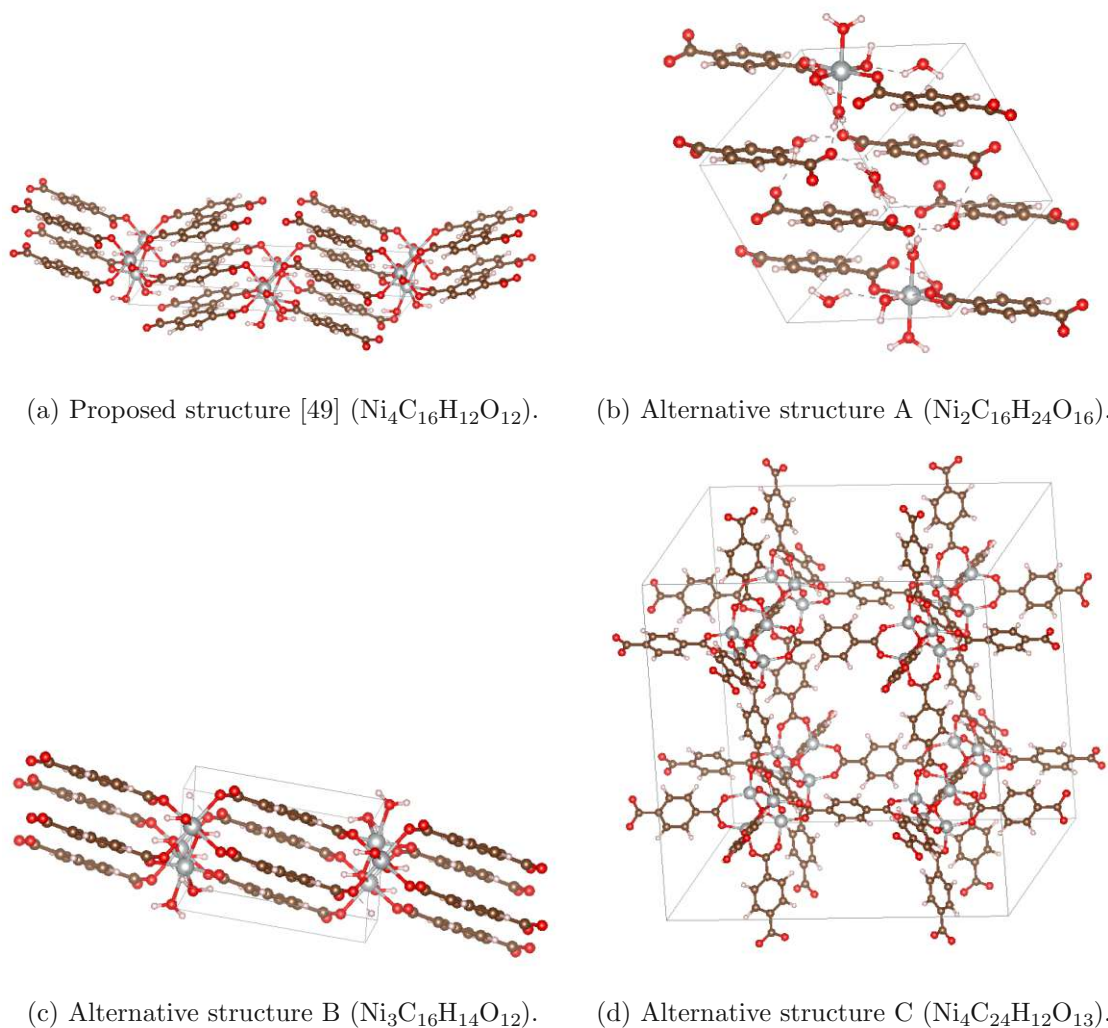(d) Alternative structure C ($Ni_4C_{24}H_{12}O_{13}$).

Figure 3.1: Possible structures for the MOF studied here consisting of terephthalic acid linkers and Ni ions. Ni atoms in gray, C atoms in brown, O atoms in red, and H atoms in white.

subsequent grid levels have an energy cutoff corresponding to

$$E_{cut}^i = \frac{E_{cut}^1}{3^{(i-1)}}, \tag{3.1}$$

meaning that the coarseness of all grid levels is defined by this parameter.

The Gaussians are subsequently mapped onto the grids. The idea of the multi-level grid is that each Gaussian, wide or narrow, is mapped onto a grid, where it covers about the same number of grid points. The REL_CUTOFF parameter defines a reference grid and the Gaussians are then mapped onto the coarsest grid level on which they cover an equal or greater number of points than covered on the reference grid.

Both parameters must be adjusted to give reasonable results. If the CUTOFF is too low then all grid levels will be coarse. If REL_CUTOFF is too low, all Gaussians will be mapped onto the coarsest grid, not taking advantage of the finer grids [56].

To determine an appropriate cutoff value for the MOF structures, calculations with CUT-OFFs from 500 Ry to 2000 Ry were done. To give an example of the results of this process the calculated total energy and the number of Gaussians mapped on each grid level were plotted for the alternative structure B and can be seen in Fig 3.2.

For the smaller cutoffs, all grids are so coarse that most Gaussians are mapped to the finest grid level 1. In this case, with a cutoff of 1000 Ry an accuracy of 10^{-3} Ry is reached, which is low compared to the recommended 10^{-6} [56]. Considering the size of the cell, which contains 810 atoms, the accuracy was deemed reasonable, given the necessity to make trade-offs with computational time. Similar plots for the REL_CUTOFF parameter can be seen in Fig. 3.3 where values from 10 Ry to 100 Ry were attempted.

As mentioned previously, for low values of REL_CUTOFF most Gaussians are mapped to the coarsest grid (level 4), while higher values lead to an increase in the number of Gaussians mapped to the finest grid. Based on these calculations for structure B, a CUTOFF of 1000 Ry and a REL_CUTOFF of 50 Ry were used for further calculations. These values were chosen as they yield well-converged total energy results and efficiently utilize all grid levels available.

After determining the cutoff values for each of the four structures, a cell optimization was performed in order to obtain the relaxed structures. Additionally, the projected density of states was analyzed to gain initial insights into the electronic structures of the MOFs.

3.2 Monolayer MoS$_2$

This study employed Density Functional Theory calculations to investigate the response of MoS$_2$ monolayers to strain using the Quantum ESPRESSO (QE) package [38], [39]. As the choice of exchange-correlation functional, the used pseudopotentials, and the inclusion of spin-orbit coupling (SOC) are known to influence the results of *ab initio* calculations, different combinations were investigated within the scope of this thesis. The LDA [30] and PBESOL [33] exchange-correlation functionals were used in combination with ultra-soft pseudopotentials (USPPs). The PBE [32] functional was used in four different variations; one using a norm-conserving potential, produced using the Optimized Norm-Conserving Vanderbilt Pseudopotential code by D.R. Hamann for molybdenum (Mo) [57] and a USPP for sulfur (S) using different USPPs, one applying the PAW potentials and one including SOC while also using USPPs. All pseudopotentials were taken from the QE pseudopotential library [58].

3.2.1 Cutoff Convergence

Prior to performing the calculations necessary for determining carrier mobility, a systematic convergence analysis was conducted for key parameters. The convergence analysis con-
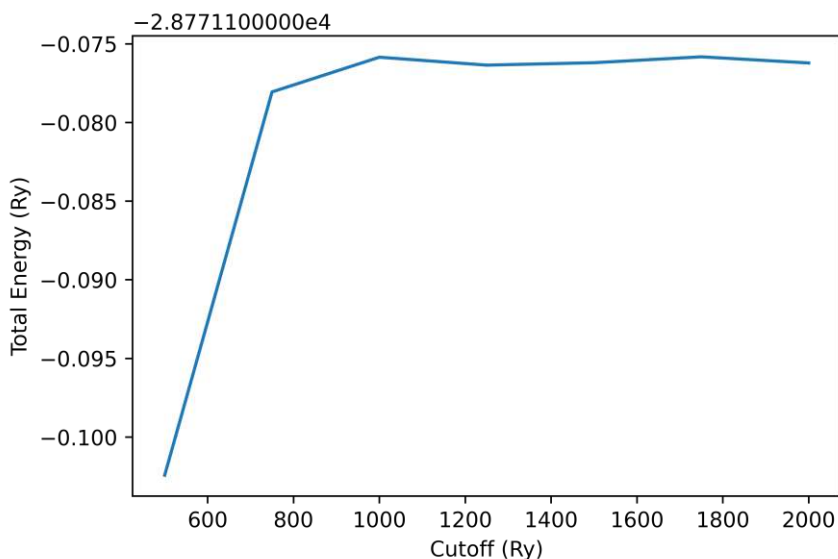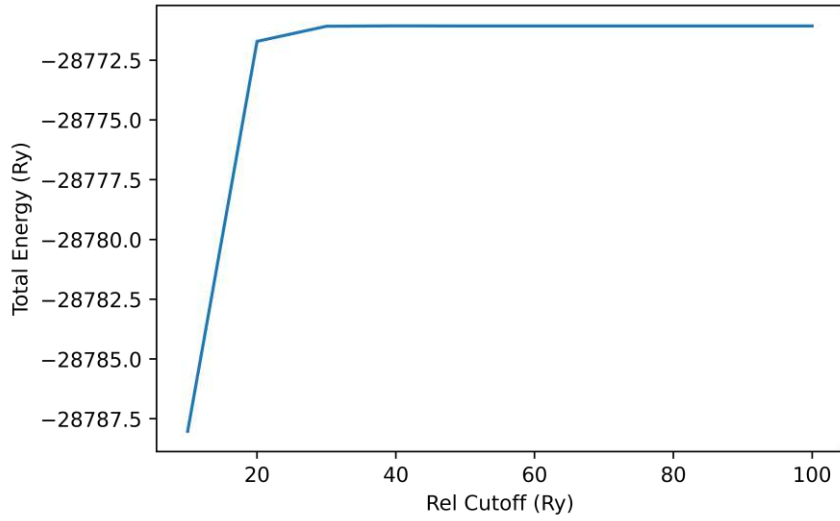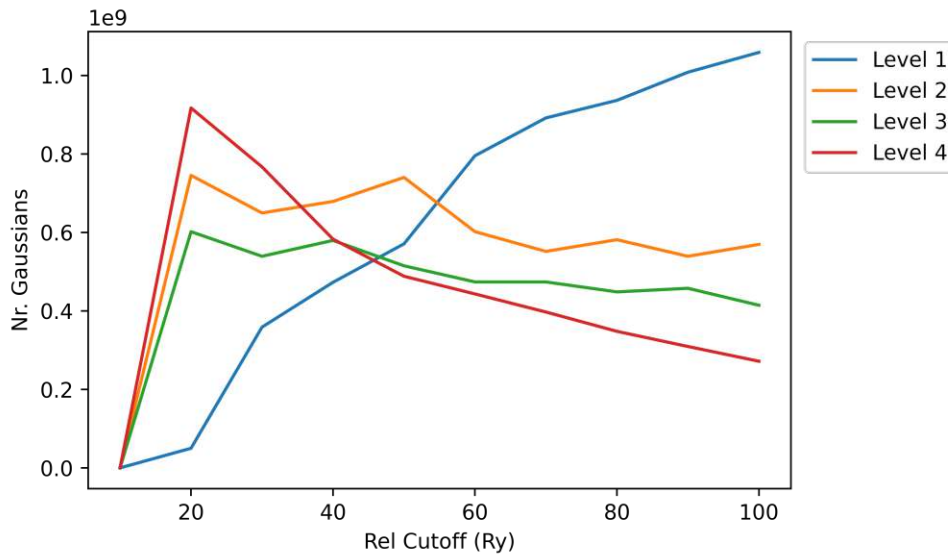
(a) Total energy dependent on CUTOFF.
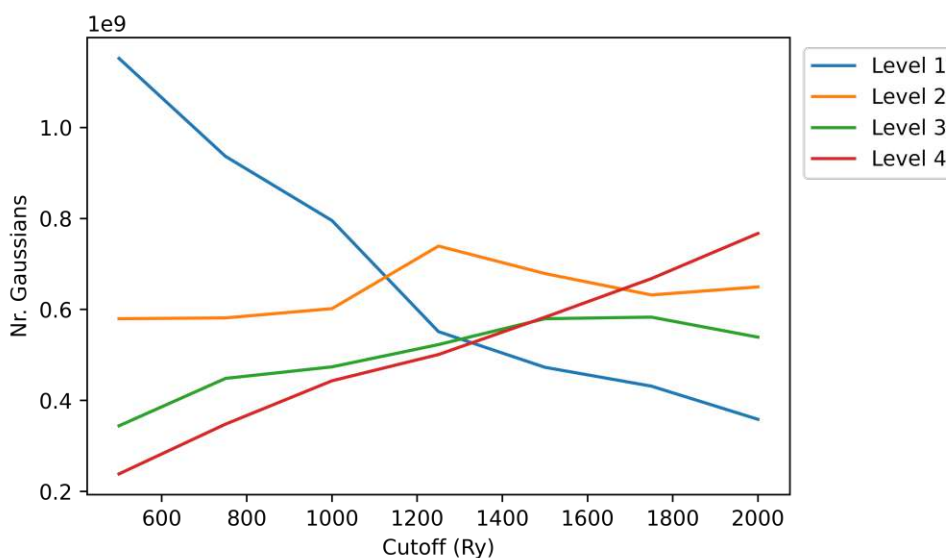
(b) Nr. Gaussians per grid level.

Figure 3.2: Convergence plots for the CUTOFF parameter in calculations of a supercell of structure B.

cerned itself with three critical parameters: the kinetic energy cutoff for the wavefunction in Ry (ecutwfc), the kinetic energy cutoff for charge density and potential in Ry (ecutrho), and the k-point grid. The ecutwfc parameter was varied across a range of values, from 20 Ry to 100 Ry. Subsequently, the ecutrho parameter was assessed, with values ranging from 300 Ry to 1000 Ry, guided by recommendations from the QE input documentation of 8 to 12 times ecutwfc for ultrasoft pseudopotentials and 4 times ecutwfc for PAW datasets.

(a) Total energy depended on REL_CUTOFF

(b) Nr. Gaussians per grid level.

Figure 3.3: Convergence plots for the REL_CUTOFF parameter in calculations of a super-cell of structure B.

After finding reasonable values for ecutwfc and ecutrho, a k-point convergence analysis was performed, using grids of varying density: 8×8×1, 16×16×1, 32×32×1, 32×32×2, and 64×64×1. Note: Due to the material being two-dimensional (2D) the grids are also kept 2D.

While varying the respective parameters, energy calculations were performed for each DFT "flavor". The resulting energy values were visualized through curves, allowing insights into

parameter convergence trends. An example is given in Fig. 3.4, showing the convergence curve for ecutwfc when performing calculations using the LDA functional.
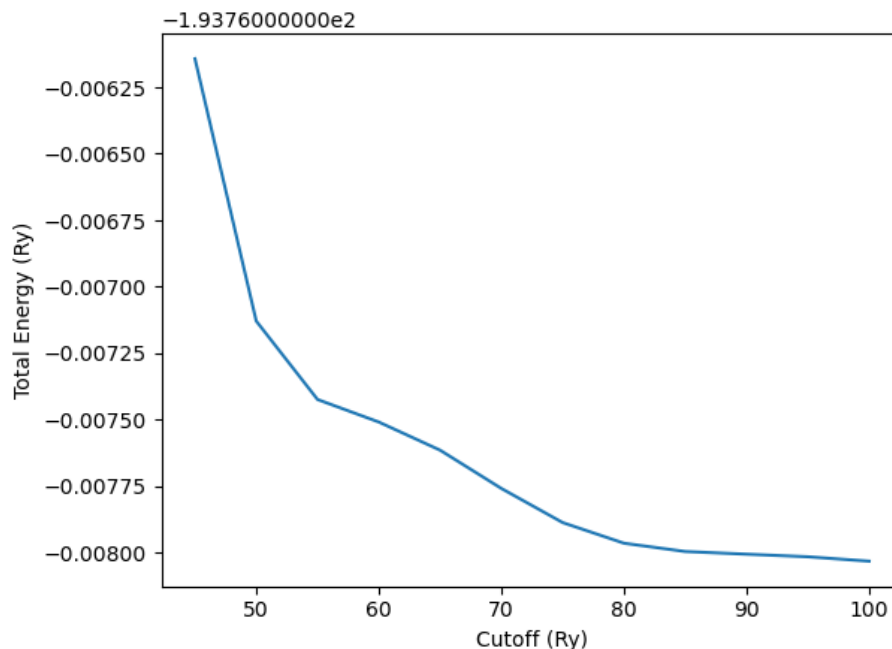

Figure 3.4: Convergence curve for ecutwfc with LDA functional.

This approach is necessary to determine parameter values which ensure that the subsequent DFT calculations are accurate and reliable, since the results should provide a solid foundation for the further investigation of MoS_2 under strain. It was found that a reasonable convergence was reached for a kinetic energy cutoff for a wave-function of 80 Ry, a kinetic energy cutoff for charge density and potential of 410 Ry, and a 16×16×1 k-point grid. These values were also chosen in an effort to have consistent values for all calculations. This has caused an unnecessarily high computational requirement for certain settings, but due to the small size of the unit cell, this can be considered negligible, as all calculations are performed within a few minutes.

3.2.2 Mobility Calculation

Using the basic simulation parameters obtained during the calculations of cutoff convergence, the steps used to determine mobility values are shown schematically in Fig. 3.5.
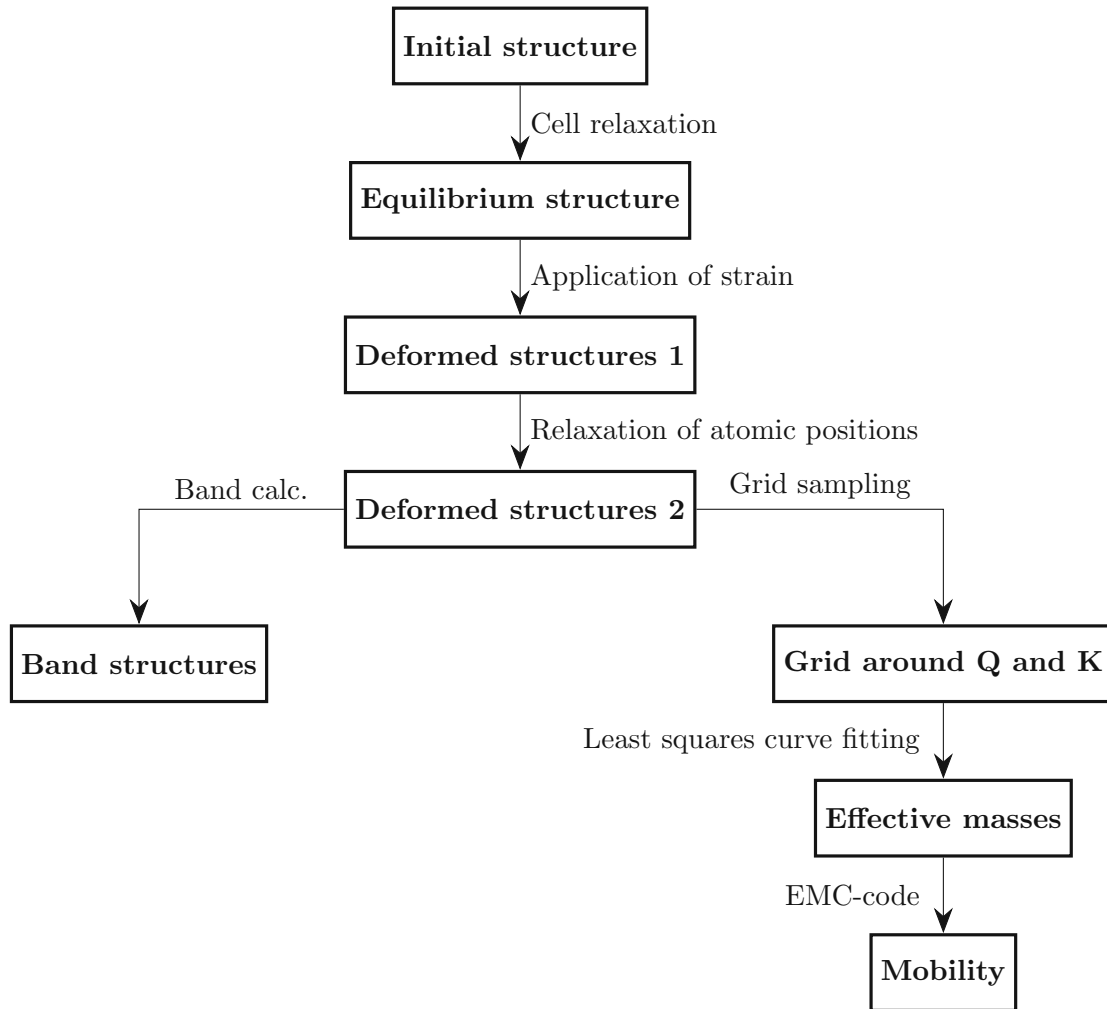
```
                    ┌─────────────────────┐
                    │  Initial structure  │
                    └─────────────────────┘
                              │ Cell relaxation
                              ▼
                  ┌───────────────────────┐
                  │ Equilibrium structure │
                  └───────────────────────┘
                              │ Application of strain
                              ▼
                  ┌───────────────────────┐
                  │ Deformed structures 1 │
                  └───────────────────────┘
                              │ Relaxation of atomic positions
       Band calc.            ▼            Grid sampling
         ┌────────┌───────────────────────┐──────────┐
         │        │ Deformed structures 2 │          │
         │        └───────────────────────┘          │
         ▼                                            ▼
┌──────────────────┐                    ┌──────────────────────┐
│ Band structures  │                    │  Grid around Q and K │
└──────────────────┘                    └──────────────────────┘
                                  Least squares curve fitting │
                                                              ▼
                                        ┌──────────────────────┐
                                        │   Effective masses   │
                                        └──────────────────────┘
                                             EMC-code │
                                                      ▼
                                           ┌──────────────┐
                                           │   Mobility   │
                                           └──────────────┘
```

Figure 3.5: Workflow for the calculation of carrier mobility in a suspended MoS$_2$ monolayer.

The detailed workflow which was employed for each pre-established combination of exchange-correlation functionals and pseudopotentials unfolds as follows:

- **Structure Relaxation:** Starting with the initial hexagonal unit cell, including three atoms, characterized by the cell parameters a = 3.16 Å and c = 37.9204 Å, a cell relaxation was performed. The reason for the magnitude of the c-parameter is that its principal intent is to include sufficient vacuum to treat the material as 2D, as opposed to bulk. Since the cell boundaries are periodic, this means that about 37 Å of vacuum is placed between successive monolayers, which is sufficient to ensure that there are no undesirable forces felt from neighboring layers [59]. During this step, the forces are systemically minimized by changes in the cell parameters and atom positions. The result is an equilibrium structure, specific to the chosen functional, capturing distinct under-/over-estimations of chemical bond strength, often manifesting as over-/under-binding.

- **Strain Application:** Subsequently, the desired strain is 'applied' to these structures by multiplying the cell parameters by a strain factor and thus deforming the cell. Biaxial strain was applied to the MoS_2 plane to ensure that the symmetry is preserved. This is vital for the subsequent scattering models implemented in the EMC code, as this approach does not consider non-degenerate Q and K valleys in the system.

- **Secondary Relaxation:** In this step only the atoms were permitted to relax, while the cell parameters remained fixed. If the cell had been allowed to relax, it would have returned to the equilibrium structure, nullifying the previous step.

- **Band Structure and Effective Mass Determination:** The resulting strained structures are then used for two further steps: First the band structure is determined, traversing the irreducible Brillouin zone from Γ to symmetry points M, K, and back to Γ. These band structures allow for the visualization of the impact of strain on the electronic structure of the material. Furthermore, the strained structures were used to determine the effective masses.

- **Effective Mass Extraction:** For the Armchair direction in the Irreducible Brillouin Zone (IBZ), following the path of the band calculations, the effective masses could also be determined based on the previous calculations, but the ellipticity of the Q valley makes it necessary to use a grid in the plane of the 2D material and fit both longitudinal and transversal effective masses at the same time. This is performed for the valleys at K and Q separately. The energy values of the conduction band are fitted to the **k** values of the phase-space using equation (2.24) with a least squares method, described in section 3.2.3.

- **Mobility calculation with the EMC code:** Finally, the effective masses, the non-parabolicity factors, and the energy difference between the K and Q valley are fed into the EMC code, and a simulation is performed to determine the carrier mobility.

3.2.3 Effective Mass Extraction

As mentioned earlier, accurately describing the elliptical shape of the Q valley, as depicted in Fig. 3.6, and confirming the expected spherical shape of the K valley, requires more than just the usual band calculations.

It is necessary to sample the Irreducible Brillouin Zone (IBZ) in two dimensions using a grid. The selection of the grid's extent and positions plays a crucial role in obtaining accurate results. For each grid, the center is established at the positions of high symmetry points K and Q. Experiments were conducted to determine the number of points and the spacing of the grids which provide a suitable empirical fit, while keeping the computational requirements at a reasonable level. Ultimately, a grid size of 19×19 was adopted, with a spacing of 1/150 in Cartesian **k**-space coordinates, as can be seen in Fig. 3.7.

This grid serves as a basis for the actual fitting: For the strained structures the bottom of the valley, that is its energy minimum, can slightly deviate from the positions of the K and Q points. Consequently, a more focused 7×7 subgrid was introduced, see Fig. 3.8.
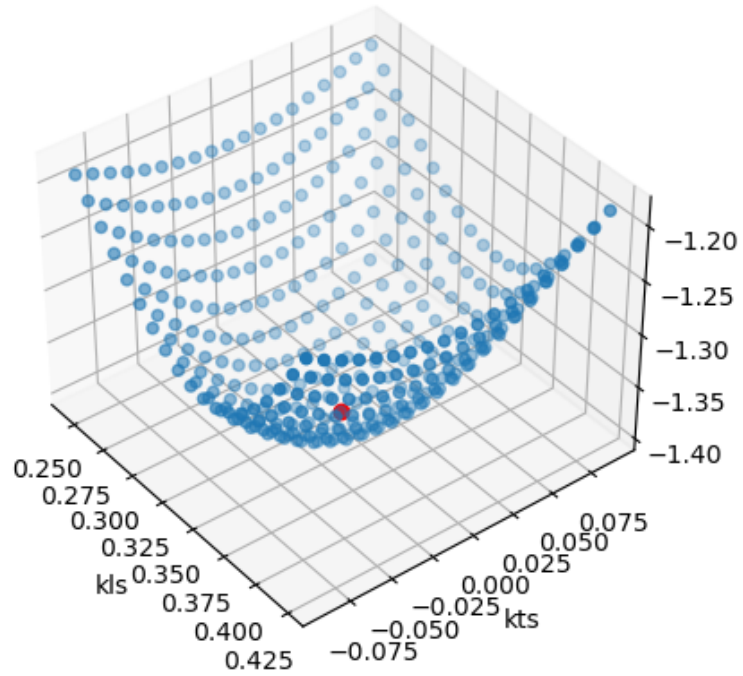
Figure 3.6: Conduction band energies at the Q valley surface.
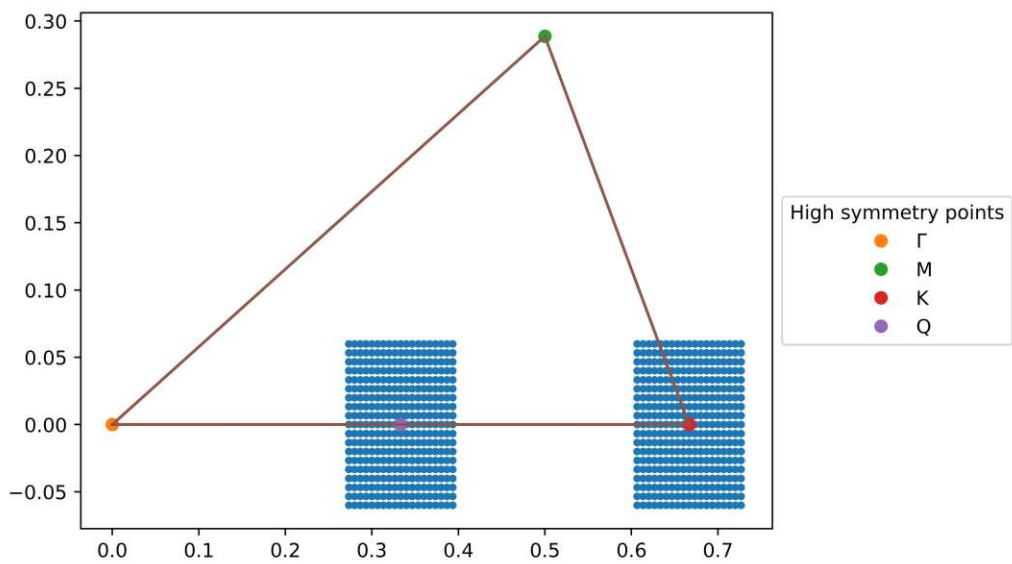

Figure 3.7: Grids centered around the K and Q point on the irreducible Brillouin zone.

The subgrid's purpose is to capture the local behavior of the valleys and encompasses the points surrounding the actual energy minima.
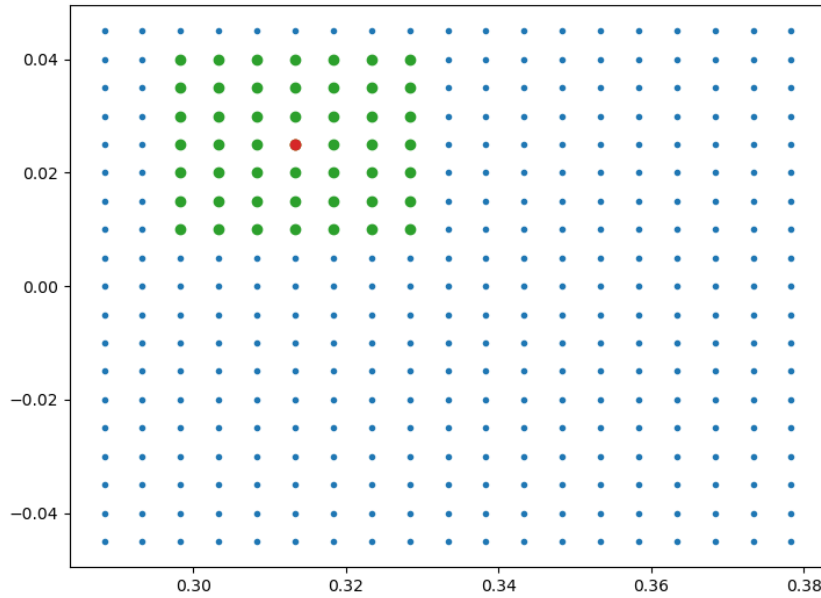

Figure 3.8: Visualisation of a 7×7 subgrid on a 19×19 base grid with the subgrid center marked in red.

The coordinates of these points, along with their respective energies of the conduction band, were then utilized to calculate the effective masses using the NumPy least squares function [60].

4 Results and Discussion

4.1 Metal-Organic Frameworks

As discussed in the implementation chapter (Chapter 3) calculating the MOF structures proved to be challenging due to its complexity, the size of the supercells of up to 810 atoms, as well as the computational time requirement. Consequently, this thesis focuses on presenting the projected density of states (PDOS) of the structures and the outcomes of the structure optimization process. The relaxed structure of the material provides information about the equilibrium positions of the atoms, helping to determine whether the structure is in a stable configuration. On the other hand, the PDOS offers insights into the electronic structure, specifically the distribution of electronic states with respect to energy levels. It also helps to identify the material's electronic properties, such as whether it behaves as an insulator, semiconductor, or metal, by examining the presence or absence of a band gap. The potential for further investigations remains, which however lie beyond the scope of this work.

The first investigated structure was proposed in a paper by Zhao et al. [49]. The initial structure compared to the optimized structure can be seen in Fig 4.1.

In this structural configuration, the coordination number of the Ni ion is six, with the Ni ion bonded to four different organic linkers and two hydroxides each. Further, it is interesting to note that the organic linkers are parallel to each other in the plane of the aromatic rings. Their arrangement contributes to the stability of the MOF which makes it necessary to take the interactions between the linkers into consideration. This is an important point as the van der Waals interactions have a long- to medium-range nature which is not per default correctly reflected in DFT as LDA and GGA neglect these non-local long-range correlations by design [61]. The PBE0 hybrid functional used for the calculations might not correctly account for these forces leading to incorrect predictions for the structures.

In order to compare the structures the focus was put on specific key parameters, which are provided in Table 4.1. These include the cell parameters, which provide insights into the MOF's overall geometry. Additionally, the shortest distance between the linker layers is examined, which is meant to reflect the limitation of the maximal pore size of the material as this is a characteristic property of the MOF material class and essential for its application. Lastly, the length of the metal ion bonds is investigated as significant changes were observed in the process of the structure optimization.

The shift in the structure seen in Fig. 4.1 is also reflected by the cell parameters. While the complex bonds of the Ni ions have become shorter, the expanded cell size suggests that, in comparison to the initial structure, there has been an underestimation of the Ni-O
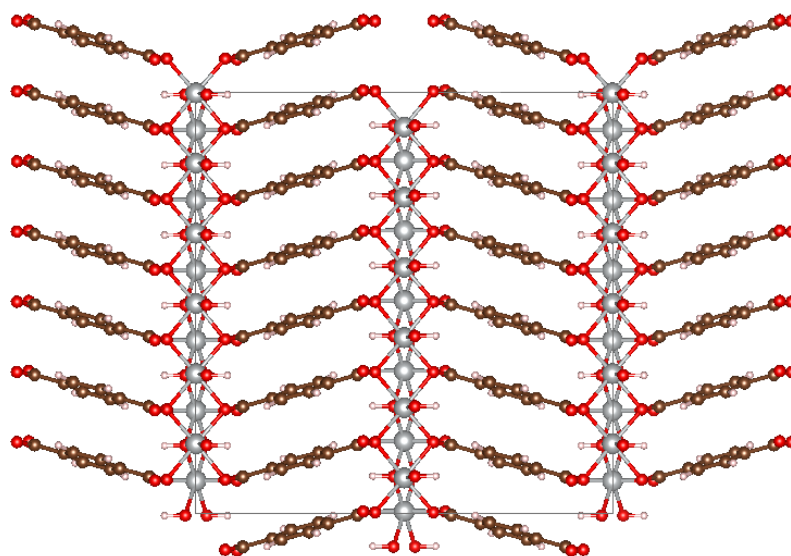
(a) Initial structure.
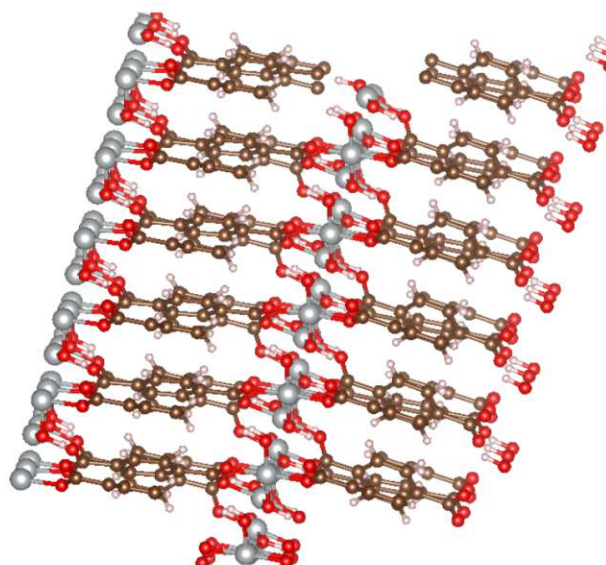
(b) Structure after cell relaxation.

Figure 4.1: The proposed MOF structure ($Ni_4C_{16}H_{12}O_{12}$) before and after cell relaxation calculations. Ni atoms in gray, C atoms in brown, O atoms in red, and H atoms in white.

interactions and an overestimation of the bond strength within the organic linkers. The angles within the framework have changed visibly, increasing the distance between the

Table 4.1: Parameters of MOF before and after cell optimization

Property	Initial structure	Final structure
Unit cell dimensions (a,b,c) in Å	19.84, 19.91, 18.80	22.75, 23.25, 19.93
Unit cell angles (α, β, γ)	90.00, 96.55, 90.00	113.083, 110.98, 73.13
Cell volume Å^3	7379.68	8916.86
Linker-layer distance in Å	3.32	3.88
Ni-linker bond in Å	2.15-2.20	1.86
Ni-OH bond in Å	1.98	1.85

linkers. The terephthalic acid linkers have twisted away from each other as direct stacking is causing repulsion between the aromatic rings.

The projected density of states was determined for the geometrically optimized structure and is plotted in Fig 4.2. Beside the energy range shown in Fig 4.2 some nickel energy states can be found at low energies between -70 eV and -60 eV. Otherwise, nickel dominates the states between -20 eV and -10 eV and around -6 eV and 4 eV. Oxygen shows a high density of states near the valence band, carbon dominates around -4 eV. The band gap of 3 eV indicates possible optical activity in the vis spectrum, which is a desirable trait for sensors. This also suggests non-conducting behavior.

The result of the geometry optimization of the first alternative structure for the MOF is shown in Fig 4.3. In this structure, the coordination number of the Ni ion is still six, but now it bonds with only two organic linkers and four water molecules each. Furthermore, in this structure, water appears as an essential structural element, introducing hydrogen bonds as a further mode of interaction which poses a challenge to the conventional density functional. Unlike the structure discussed before, the linker layers remain parallel to each other, even after the cell optimization, but at a much longer distance. The coordination number in the optimized structure is reduced to four as two water molecules move further away.
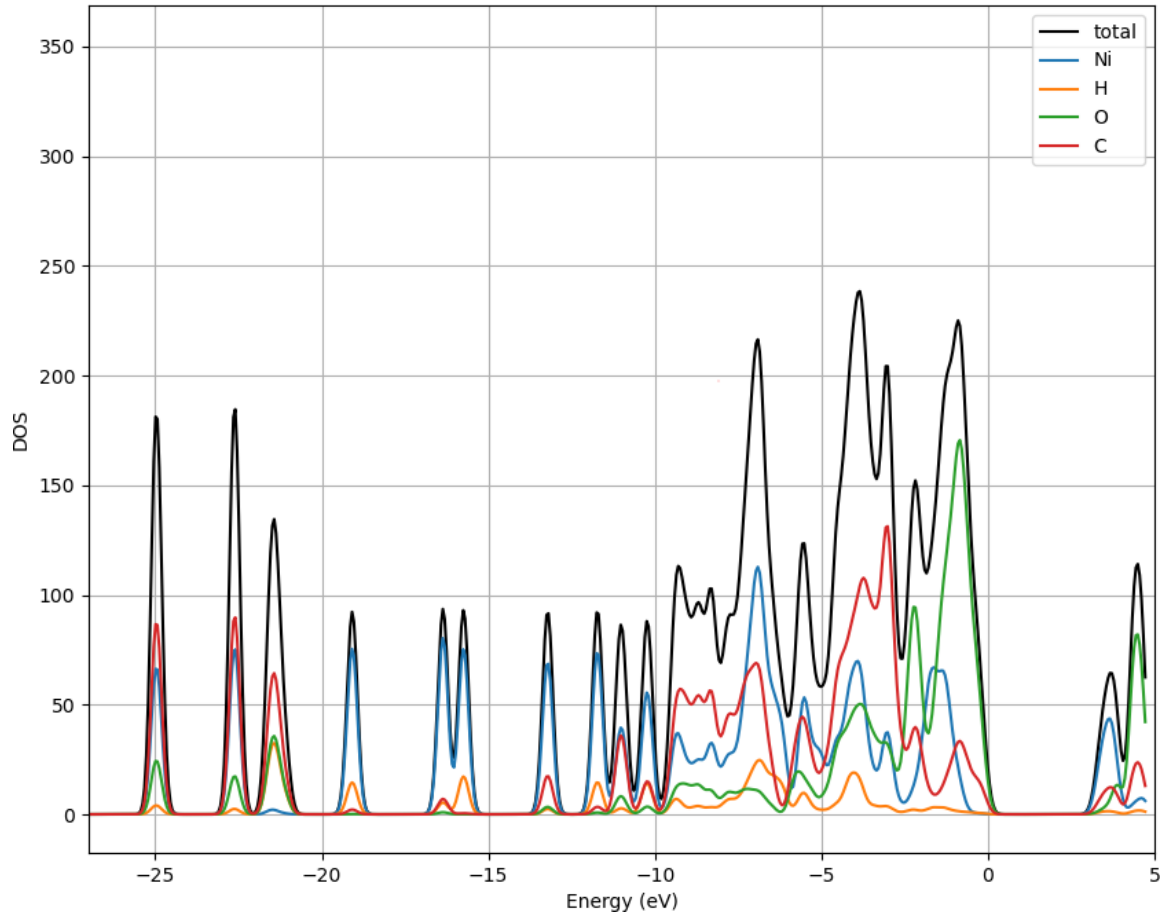
Figure 4.2: Calculated PDOS for the proposed structure.

Table 4.2: Parameters of MOF A before and after cell optimization

Property	Initial structure	Final structure
Unit cell dimensions (a,b,c) in Å	16.94, 17.61, 17.61	17.56, 18.69, 18.85
Unit cell angles (α, β, γ)	99.41, 109.39, 109.39	109.67, 106.17, 105.84
Cell volume $Å^3$	4444.45	5116.77
Linker-layer distance in Å	3.42	4.49
Ni-linker bond in Å	2.08	1.85
Ni-water bond in Å	1.99-2.15	1.88

The parameters in Table 4.2 show that the edge lengths (a,b,c) of the cell increase. Additionally, the distance between the linker layers increases, ultimately leading to larger pores. As observed earlier, the complex bonds of the Ni ions all seem to become shorter.

The projected density of states for structure A is plotted in Fig 4.4. There is a high density of states for nickel outside the shown interval at -70 eV and -60 eV. The states between -20 eV and -10 eV are dominated by carbon, as well as the states near the valence and
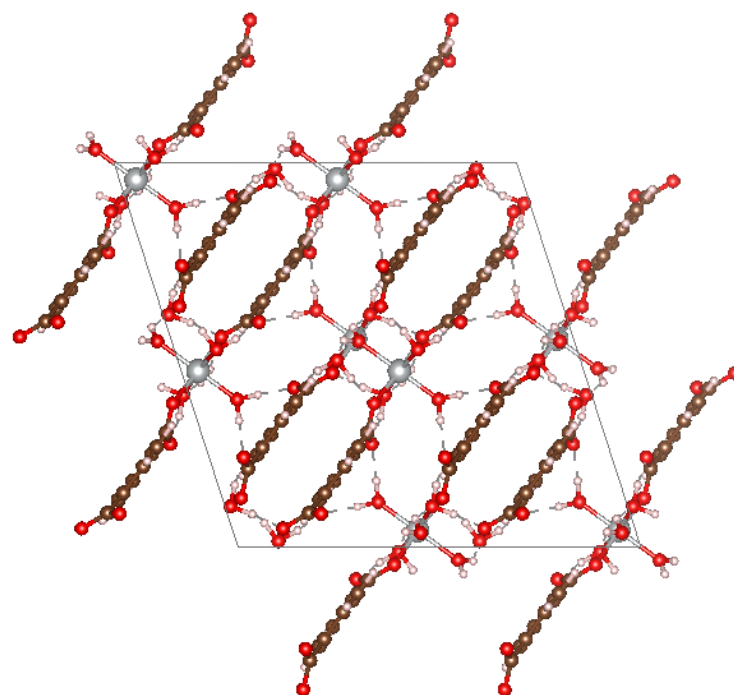
(a) Initial structure.
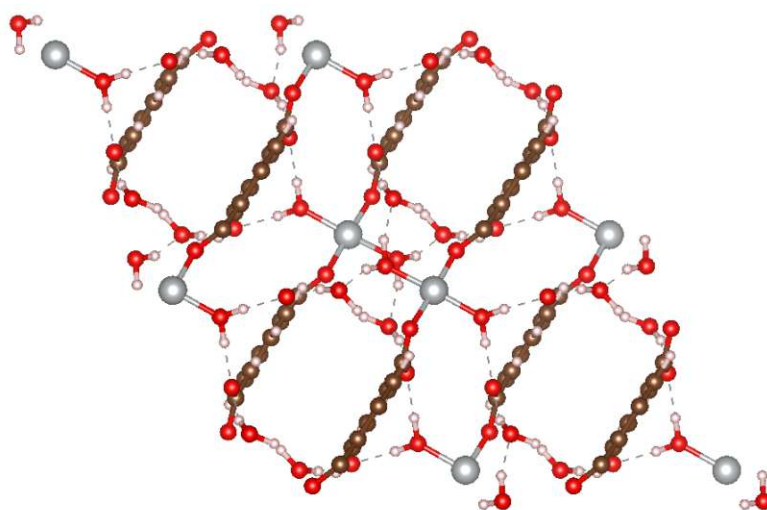
(b) Relaxed structure.

Figure 4.3: The alternative A MOF structure ($Ni_{12}C_{16}H_{24}O_{16}$) before and after cell relaxation calculations.

conduction band. An even higher band gap of about 5 eV is indicated for this material.

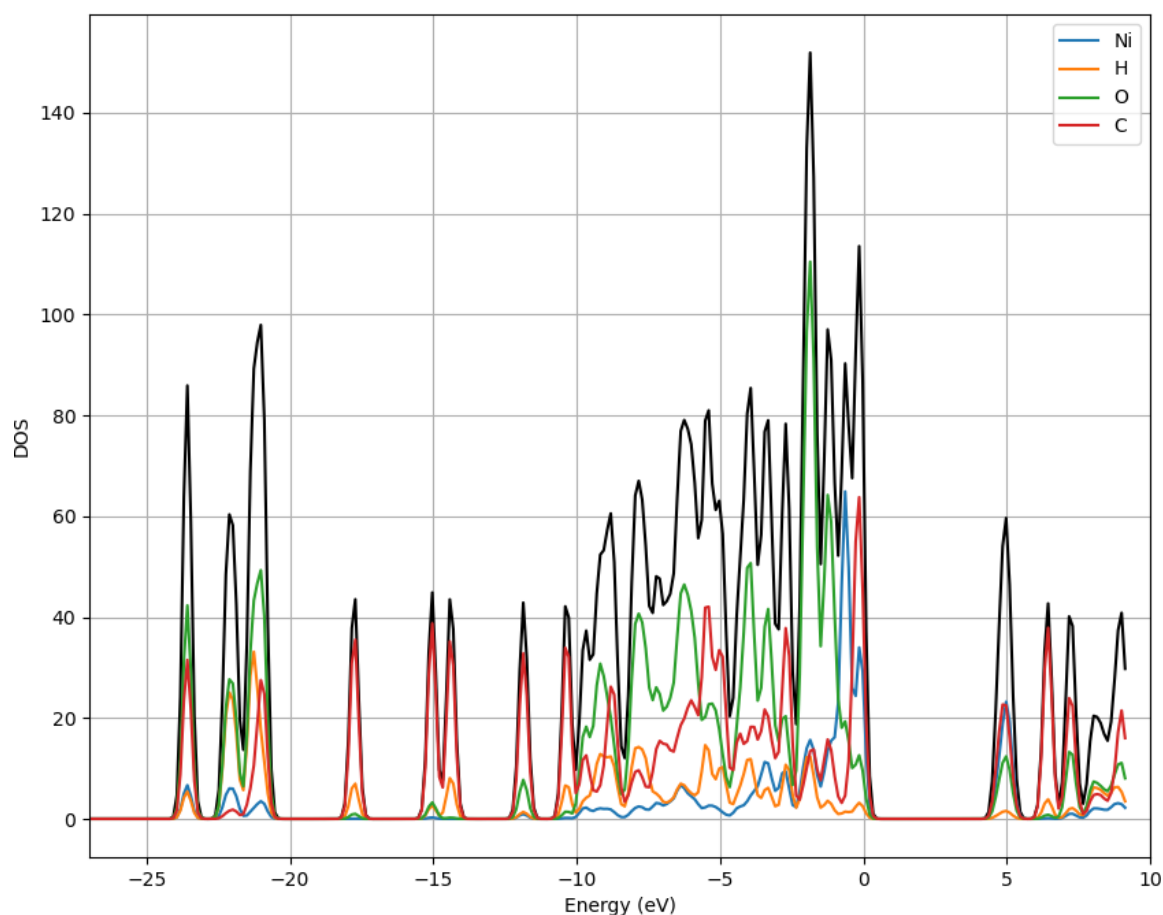The result of the geometry optimization of the alternative structure B is shown in Fig 4.5.

Figure 4.4: PDOS of structure A.

Structure B is very similar to the initial proposed structure, with one essential difference: there are two types of Ni ions present. One is very similar to those in the first structure, with a coordination number of six and bonded to four terephthalic acid linkers and two hydroxides. The other one also has a coordination number of six, but it is bonded to only two organic linkers, two hydroxides, and two water molecules which again introduce hydrogen bonds into the structure. These two Ni types are alternating, creating a structure in which the angles between Ni ions and terephthalic acid linkers are different compared to the original structure.

The cell parameters for structure B are given in Table 4.3, and the bond lengths are given for the Ni atoms which are bonded to all three types of ligands. In this structure, the cell undergoes both a reduction in size and distortion. The terephthalic acid linkers move away from each other, while the complex bonds become more tightly bound.

The projected density of states for structure B is plotted in Fig 4.6. This PDOS plot has similarities with the one of structure A. However, while for A the energy states near the valence band are dominated by carbon, for structure B it is nickel that predominates. For
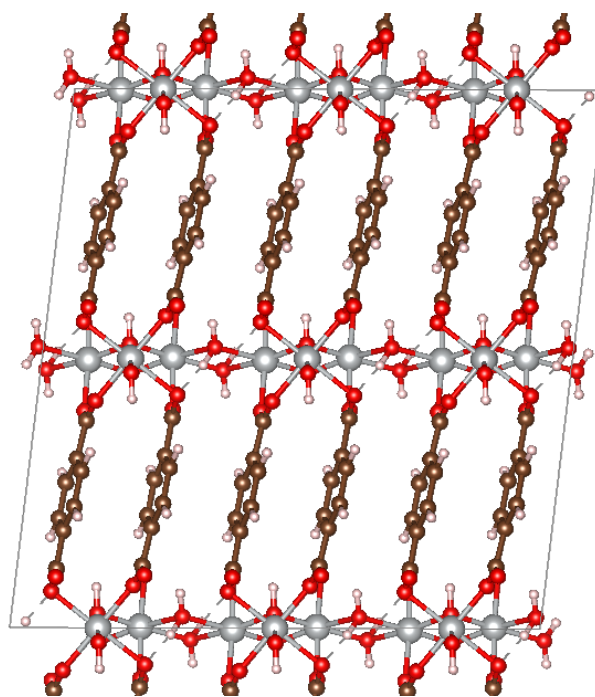
(a) Initial structure.
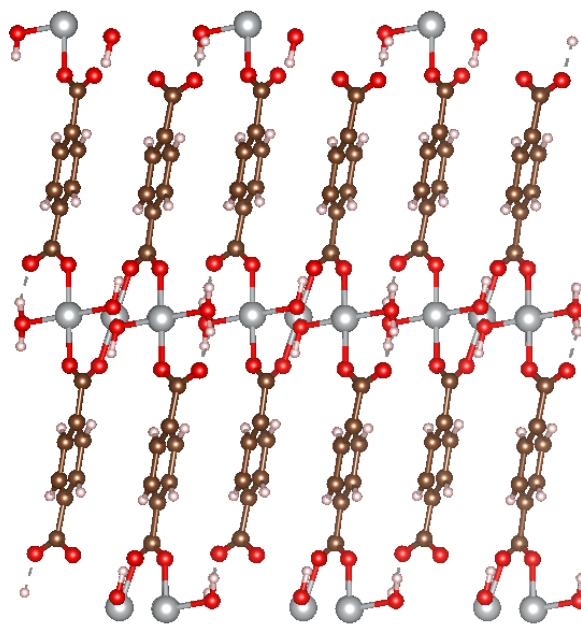
(b) Relaxed structure.

Figure 4.5: The alternative B MOF structure ($Ni_3C_{16}H_{14}O_{12}$) before and after cell relaxation.

Table 4.3: Parameters of MOF B before and after cell optimization

Property	Initial structure	Final structure
Unit cell dimensions (a,b,c) in Å	18.59, 19.87, 20.41	23.23, 24.72, 22.72
Unit cell angles (α, β, γ)	82.82, 83.25, 85.59	104.33, 66.79, 126.71
Cell volume Å^3	9992.53	9616.75
Linker-layer distance in Å	3.34	4.13
Ni-linker bond in Å	2.02	1.86
Ni-water bond in Å	2.21	1.89
Ni-OH bind in Å	2.05	1.83

the conduction band, carbon states come first, closely followed by nickel states.
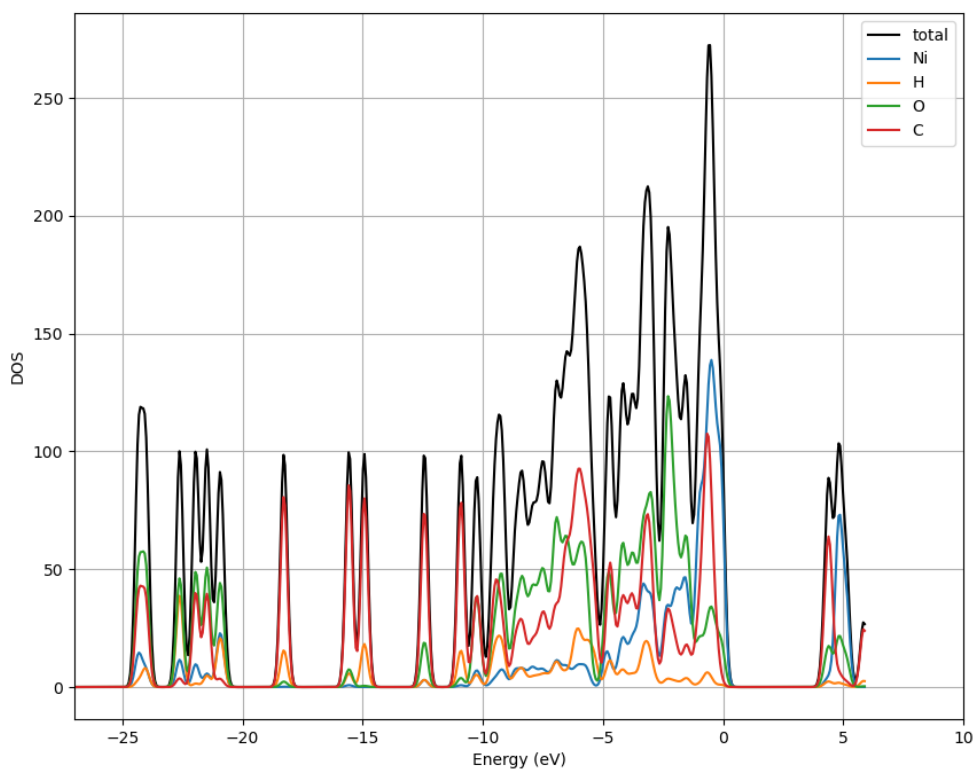

Figure 4.6: Calculated PDOS of structure B.

The result of the geometry optimization of the alternative structure C is shown in Fig 4.7. In stark contrast to the other three presented structures, this one includes Ni ions with a coordination number of four. A group of four Ni atoms is centered around a single oxygen atom which serves as a bridging ligand, while each Ni is connected to its three neighbors

by terephthalic acid linkers. This structure is very sparse and has very large pores, while also being very symmetrical.
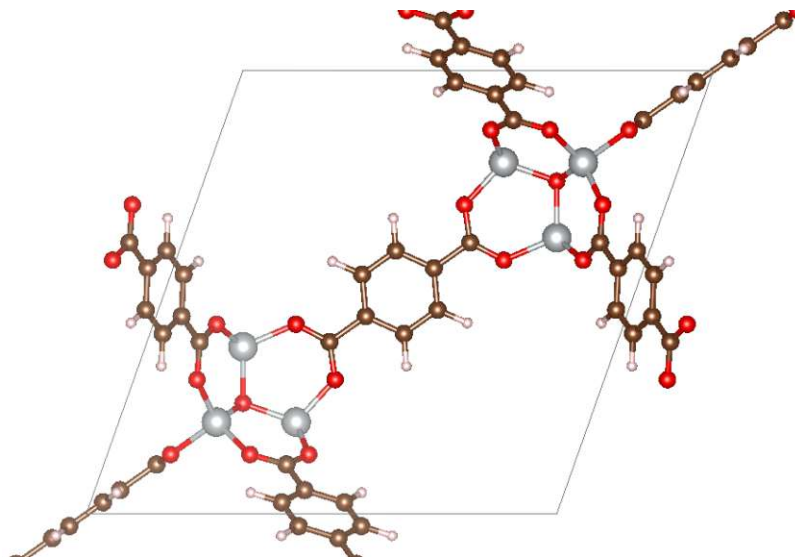
(a) Initial structure.
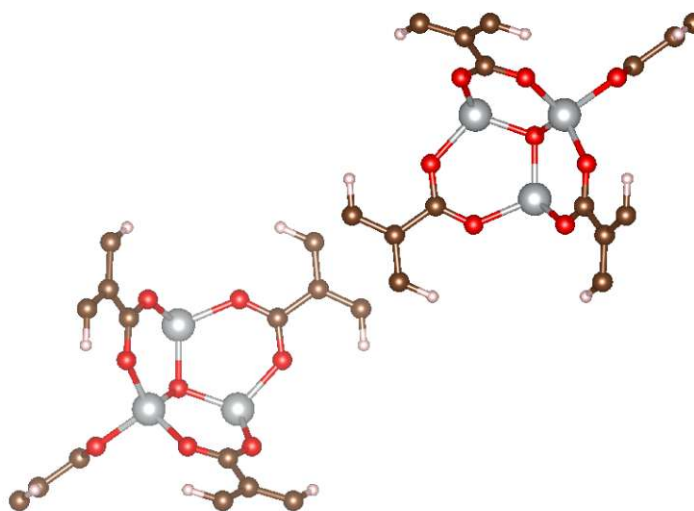
(b) Relaxed structure.

Figure 4.7: The alternative C MOF structure ($Ni_4C_{24}H_{12}O_{13}$) before and after cell relaxation.

As can be seen in Fig. 4.7 and Table 4.4, the optimization process had little effect on this structure. This can be attributed to the forces within the initial structure being already well-balanced, due to its high symmetry and its relatively sparse nature.

The projected density of states for structure C is plotted in Fig 4.8. It is clear to see that this structure is very different from the other proposed ones. Not only does it have

Table 4.4: Parameters of MOF C before and after cell optimization

Property	Initial structure	Final structure
Unit cell dimensions (a,b,c) in Å	18.25, 18.25, 18.25	18
Unit cell angles (α, β, γ)	59.99, 59.99, 59.99	60.04, 60.03, 60.03
Cell volume Å^3	4301.71	4320.71
Linker-layer distance in Å	10.73	10.81
Ni-linker bond in Å	1.89	1.87
Ni-O bond in Å	1.93	1.96

a significantly larger pore size, but the projected density of states indicates a much lower band gap, suggesting conducting or at least semi-conducting behavior.
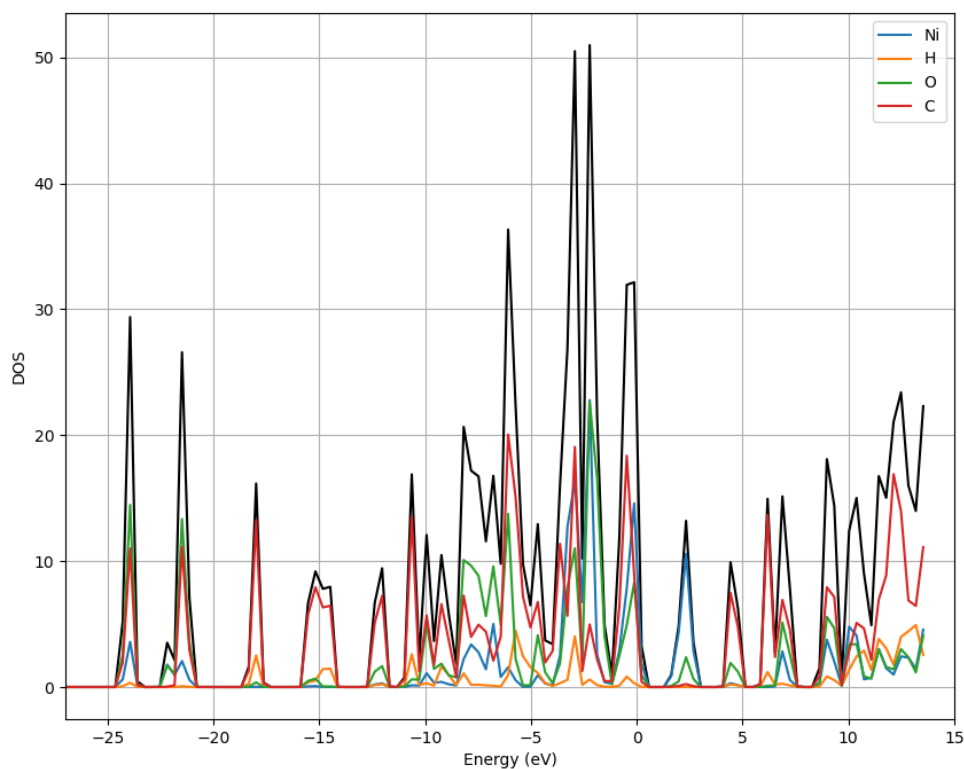

Figure 4.8: PDOS of structure C.

It is important to note that, even though in this thesis only structure optimizations are presented, these were not the initial goals of the project. The aim was to establish a practical method to calculate these structures, in order to move on from bulk materials to study surface properties and eventually, predict interactions between the MOFs and potential

analytes. As the ingredients of the synthesis method of the MOF also allowed for other potential structures, a further idea was to investigate alternative structure arrangements.

Unfortunately, the chosen *ab initio* approach turned out to be highly computationally expensive, very time-consuming, and difficult to converge. First, Quantum ESPRESSO calculations were performed, which incorrectly predicted metallic behavior. Consequently, the approach was shifted to CP2K to perform calculations with hybrid functionals in order to improve the accuracy of the electronic structure. As the calculation of the Hartree-Fock exchange is usually computationally demanding, especially for larger systems, the Auxiliary Density matrix method [62] was used. This method, implemented in the CP2K code, enables good performance and accuracy, when including Hartree-Fock exchange calculations. This boost in efficiency becomes even more important, when using supercells of the structures in order to improve convergence. Structure relaxations were conducted successfully and the projected density of states was calculated for the different structures. However, it has to be noted, that certain critical features, like the pore width, may not be accurately predicted due to insufficient considerations of Van-der-Waals forces, as previously discussed. Experimental data, such as X-ray absorption spectroscopy or X-ray diffraction, would provide more reliable characterization of the different structure geometries than solely relying on *ab initio* calculations. However, due to the lack of such experimental validation and the impracticality of the computational approach, no further investigations were pursued for these materials.

In order to use *ab inito* methods to investigate MOFs for their potential sensing capabilities a more efficient method is necessary. Also because they are such large structures it might make sense to simply look at the linkers / functional groups and how they react to certain analytes.

4.2 Molybdenum Disulfide (MoS₂)

As previously mentioned, Density Functional Theory (DFT) calculations are an established method for investigating the behavior of materials. However, the accuracy and reliability of these calculations depend on several key factors, such as the choice of pseudopotentials, exchange-correlation functionals, and which properties need to be predicted. When simulating the impact of strain on the band structure and consequently on the carrier mobility of MoS_2 monolayers, these choices lead to considerable differences in the results.

To illustrate this, some properties which emerge when calculating the equilibrium structures and the corresponding band structures for the different DFT settings, are shown in Table 4.5. Even though all calculations have the same starting point, depending on the chosen functional (LDA, PBE, PBESOL) and pseudopotential, the size of the equilibrium cell, the band gap, and the energy difference between the Q and K valleys can widely vary. This emphasizes the critical importance of careful selection and consideration of these parameters when conducting *ab initio* DFT simulations in the study of materials. It is to be noted that for the choice of different pseudopotentials (here denominated as PBE, PBE QE) and the calculations using the PBE functional with projector augmented wave

only minor differences are expected. This is because the well-established pseudopotentials used, are standardized and have been widely tested, also pseudopotentials mainly affect the treatment of core electrons which have little impact on the electronic structure.

Table 4.5: Overview of some important parameters for the strain-free structures of each DFT-flavor.

Type/ Origin	Cell parameter a (Å)	Band gap (eV)	ΔE_{QK} (eV)
LDA	3.129	1.852	0.083
PBE	3.184	1.689	0.262
PBESOL	3.142	1.806	0.151
PBE with PAW	3.185	1.678	0.267
PBE QE	3.186	1.679	0.267
PBE with SOC	3.160	1.691	0.169
Experimental	3.14 [63]- 3.169 [64]	1.8 [21]	–

When comparing the computationally determined cell parameters to their experimental counterparts it becomes evident that experiments also only allow to determine these parameters up to a certain accuracy and that different setups might yield different results. The values displayed in the table are meant to show the range of results. Nevertheless, both LDA and PBE show their known tendencies to over- and under-bind, with LDA underestimating the cell parameter and PBE overestimating the cell parameter. Even though LDA and PBESOL are remarkably close to the experimentally determined band gaps, the values are to be taken with a grain of salt as DFT generally underestimates the band gap. In this context, the band gap is only shown to illustrate the fundamental differences in the electronic structure resulting from the different calculations. This can also be seen in the large variation of the energy difference between the Q and K valleys ΔE_{QK}. This parameter plays a crucial role in determining the scatter rates in the conduction band and therefore also the carrier mobility.

The differences in the electronic structure become even more apparent when examining the band structures. In the context of the Ensemble Monte Carlo Simulations, a reasonable description of the conduction band is crucial. Fig. 4.9 presents the conduction bands resulting from various DFT calculations of the unstrained structures, where the energy on the vertical axis is given relative to the valence band maximum.

As pseudopotentials and PAW show little difference, they can be discussed under the umbrella of calculations with the PBE functional without additional considerations like spin-orbit coupling. Fig. 4.9 clearly shows that the conduction band calculated with LDA and PBESOL is similar and situated at higher energies, with LDA having the highest values, compared to the PBE-based calculations. The energy minima of the Q and K valleys are also much closer to each other, see Tabel 4.5. The influence of spin-orbit coupling becomes apparent around the Q valley and between the Γ and M symmetry points.

Evidently, the choices made, when setting up the *ab initio* DFT calculations have a great influence on the predicted electronic structure of monolayer MoS_2 before strain is even applied to the structures.
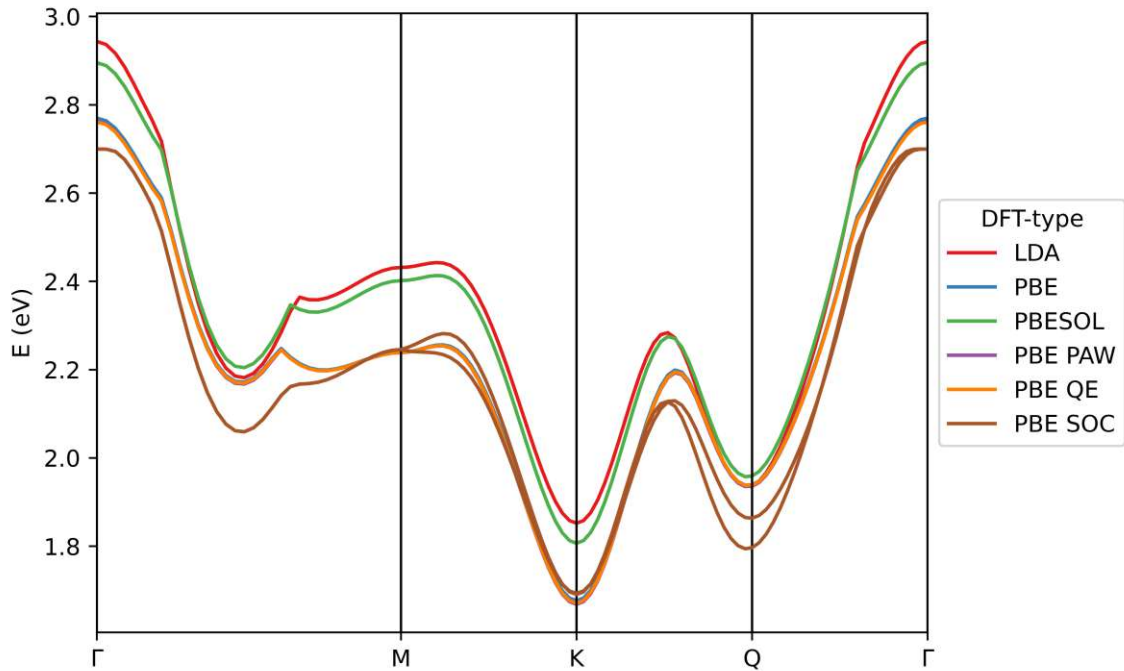
Figure 4.9: Overview: Conduction band of equilibrium structures.

To visualize the effects of biaxial tensile and compressive strains on monolayer MoS_2, compressive and tensile strains up to 5% were applied, and then the band structure was computed using the PBE functional. The results are presented in Fig. 4.10 with tensile stress indicated in blue and compressive stress in red.

Overall, a noticeable trend emerges: Under compressive strain, energy levels above the band gap tend to increase, while those below it tend to decrease. Conversely, under tensile strain, energy levels decrease across the board, particularly for those above the band gap. This trend is also reflected in the change of band gap, see Fig 4.13, when transitioning from compressive to tensile strain.

Under compressive strain, a band near the M symmetry point rises, while in the conduction band, the Q valley sinks below the K valley. This shift suggests a transition towards an indirect band gap for higher compressive strains. On the other hand, when subjected to tensile strain, the energy of the valence band at the Γ point increases, while the valence band around the K-point shows lower energies. This indicates, that with higher tensile strain, the highest energy state within the valence band will be at the Γ point, therefore also suggesting a transition toward an indirect band gap.

In the study from Deng et al. [65] biaxial symmetric compressive and tensile strains on the monolayer were investigated. Even higher amplitudes of ± 10 % strain were applied supporting the tendencies also visible in Fig 4.10. Further, the suggested transformation from a direct to indirect band gap was also reported.
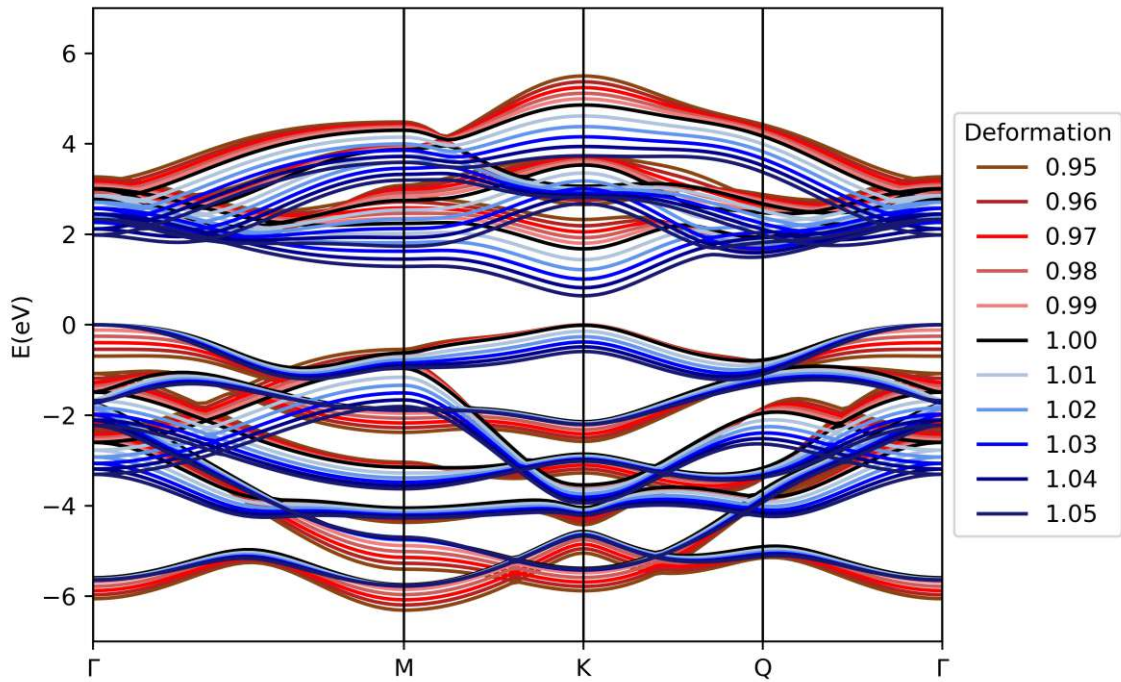
Figure 4.10: Influence of strain in the range ± 5 % on the band structure of the monolayer MoS_2 calculated with the PBE functional.

As described in the theory section in Chapter 2, the model used for simulating carrier transport and determining the mobility of strained MoS_2 relies on a multi-valley approach to approximate the conduction band. Therefore, how the application of strain influences the conduction band is especially important. To additionally showcase the dependency on the exchange-correlation functional employed for band structure calculations, Fig. 4.11 shows the conduction bands for both functionals under strains in the range ± 0.5 %.

The strains investigated in the scope of this thesis are comparatively small. The reason for this can also be explained when looking at Fig. 4.11. For LDA, the energy levels of the conduction band minima at the K and Q points approach each other with increasing compressive strain. This causes problems since the simulation is based on the assumption that the K valley is the minimum of the conduction band which is no longer true for larger compression. On the other hand, after a certain amount of tensile stress, the energy difference between the two valleys becomes so big that only very little scattering still occurs, ultimately leading to mobility values which barely change after a certain level of deformation. What is also noteworthy is that the choice of exchange-correlation functional influences how strongly the predicted conduction band reacts to the strain.

When performing DFT calculations which include spin-orbit coupling, the energy levels that would otherwise be degenerate can split. This can be observed in Fig 4.12, showing the conduction band under strain when calculations with PBE and spin-orbit coupling are performed.
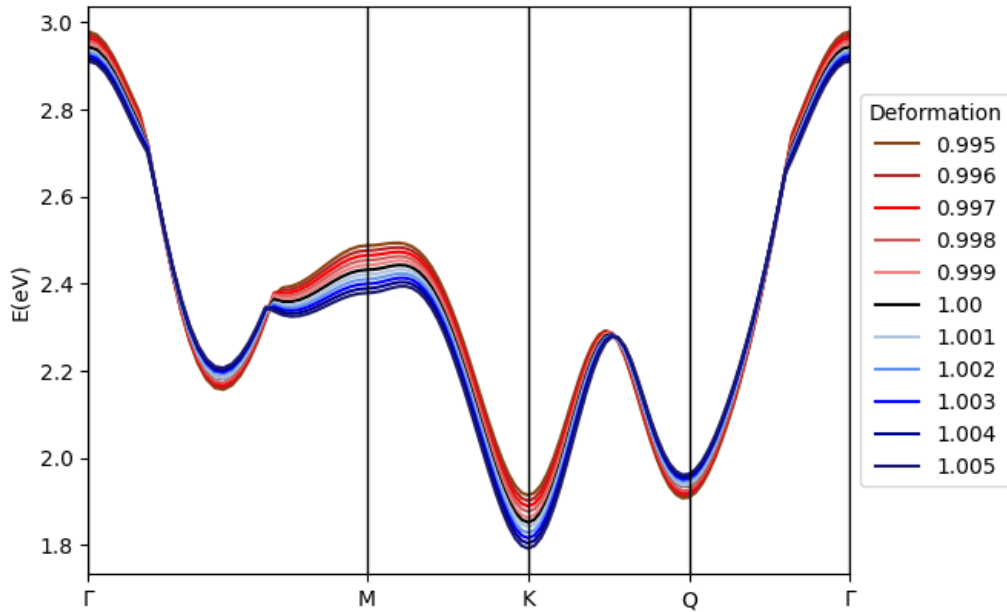
(a) LDA functional.
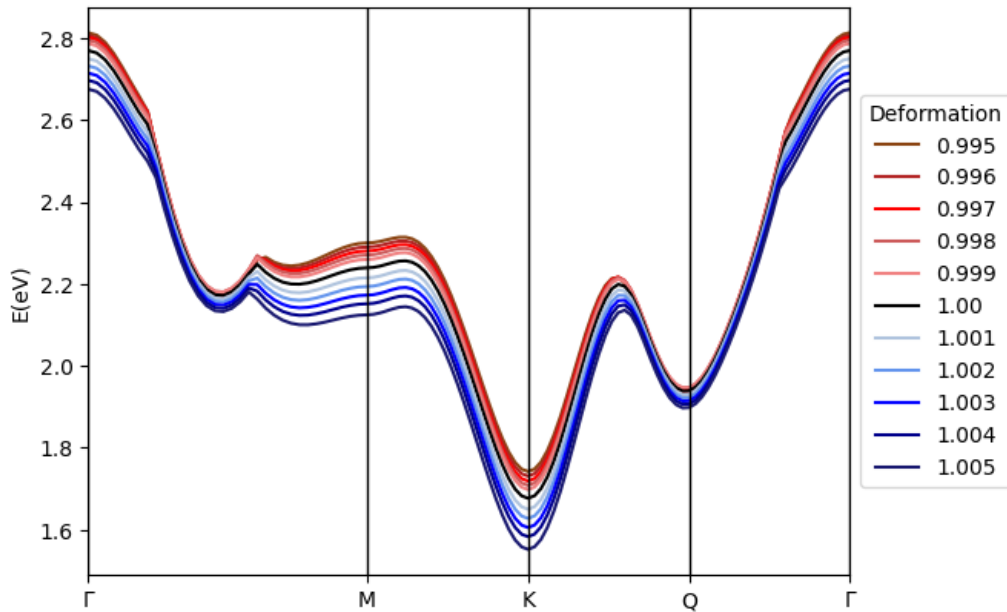
(b) PBE functional

Figure 4.11: The conduction band under strain for different functionals.

While SOC is barely noticeable at the K valley, the effect is especially pronounced around the Q valley. Here, a limitation of the model is reached, the approximation of the conduction band in the EMC code does not account for multiple non-degenerate K and Q valleys. In this case, the choice to consider SOC in the calculation is two-sided. On one hand, it can
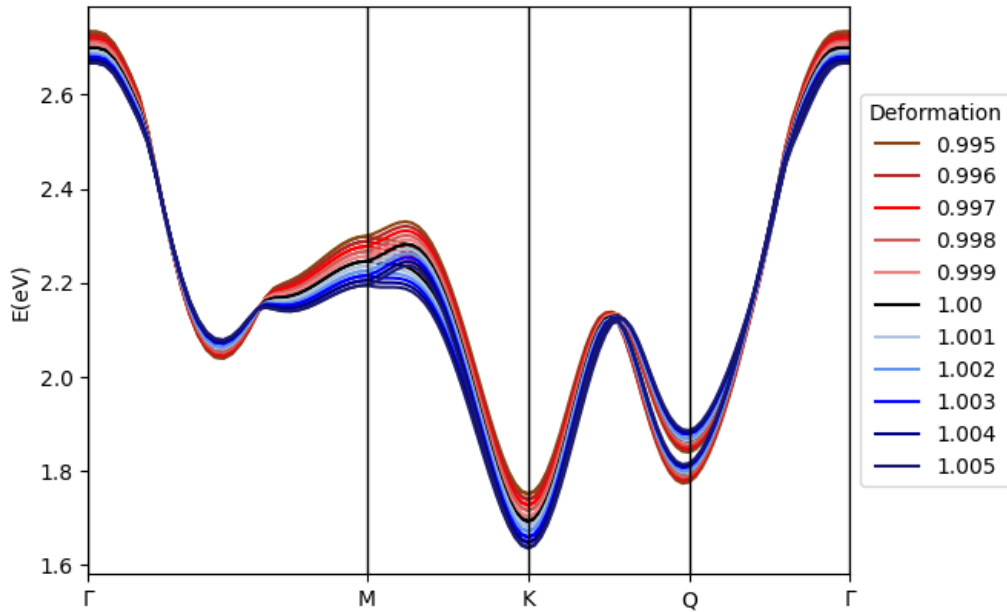
Figure 4.12: The conduction band under strain for PBE including spin-orbit coupling.

be a reasonable addition, allowing for a more realistic description of the electronic structure of the material. On the other hand, its usefulness is restricted by the simplifications made in the model into which the DFT-calculated parameters are fed. The change of the band gaps under strain, determined based on the DFT calculations, can be seen in Fig. 4.13.
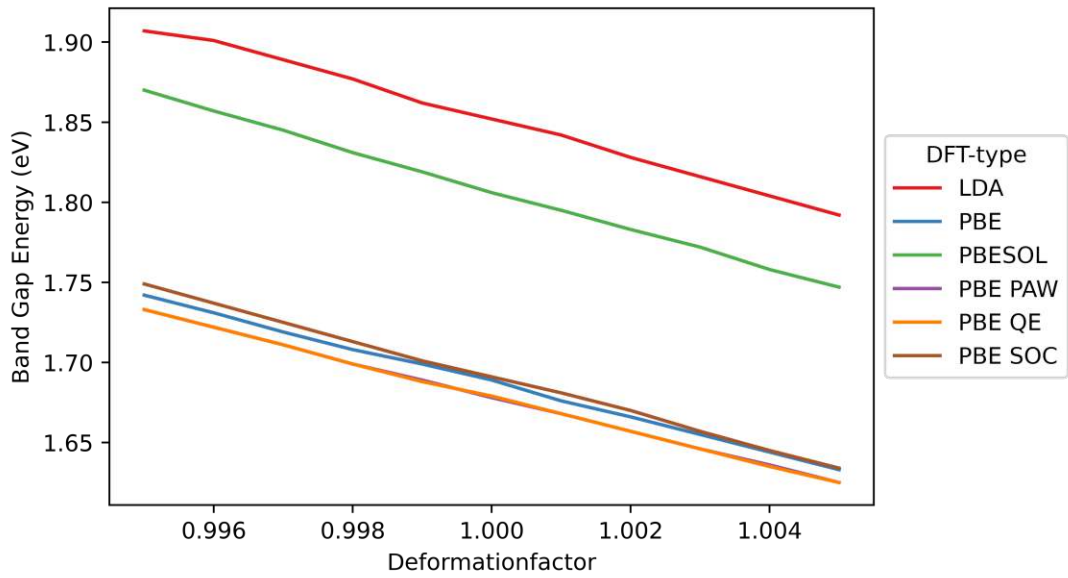

Figure 4.13: Calculated energy band gap for different DFT "flavors" under strain.

45

The calculations employing the PBE functional generally underestimate the band gap, while LDA predicts the highest one. All calculations show a decrease of the bandgap that is approximately linear at around 115 meV / % strain deformation factor.

How the application of strain affects the energy difference between the minima of the K and Q valleys can be seen in Fig. 4.14.
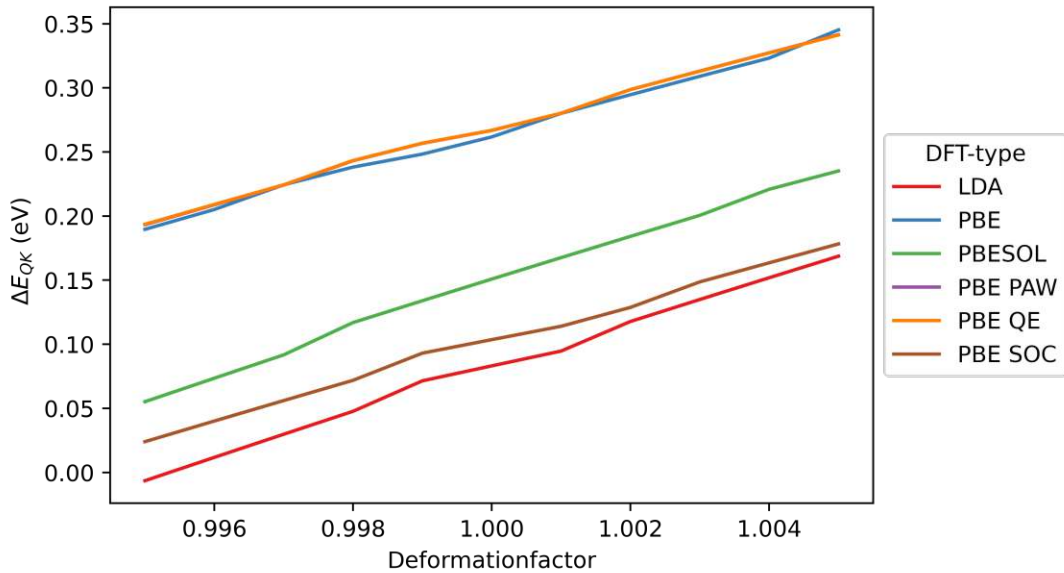

Figure 4.14: ΔE_{QK} for different DFT "flavors" under strain.

Similarly to the band gaps seen before, ΔE_{QK} has significantly different values based on the choice of exchange-correlation functional, but shows a similar near-linear dependence of about 155 meV / % on the strain. For LDA this energy difference becomes negative for strong compressive strains as the Q valley becomes lower than the K valley.

After determining the equilibrium structure, applying strain to it, and computing the band structure, the characteristics of the resulting conduction band have to be distilled down to a form suitable to be fed into the effective mass-based multi-valley approximation used in the Ensemble Monte Carlo code. This is performed by following the procedure described in Chapter 3. As an example, the results of this fitting process are shown in Fig. 4.15 for the conduction band of a PBE calculation of the equilibrium structure.

While the parabolic functions offer a reasonable approximation of the conduction band around the minima of the valleys, they quickly become inaccurate for states further away. In this case, the model is based on the assumption that the conducting electrons will be found mainly around the minima, and the curves are fitted correspondingly.

How the effective mass approximation parameters change after strain is applied is illustrated in Fig. 4.16, Fig. 4.17 and Fig. 4.18.

Fig. 4.16 illustrates the parameters used to approximate the K valley. Due to the spherical
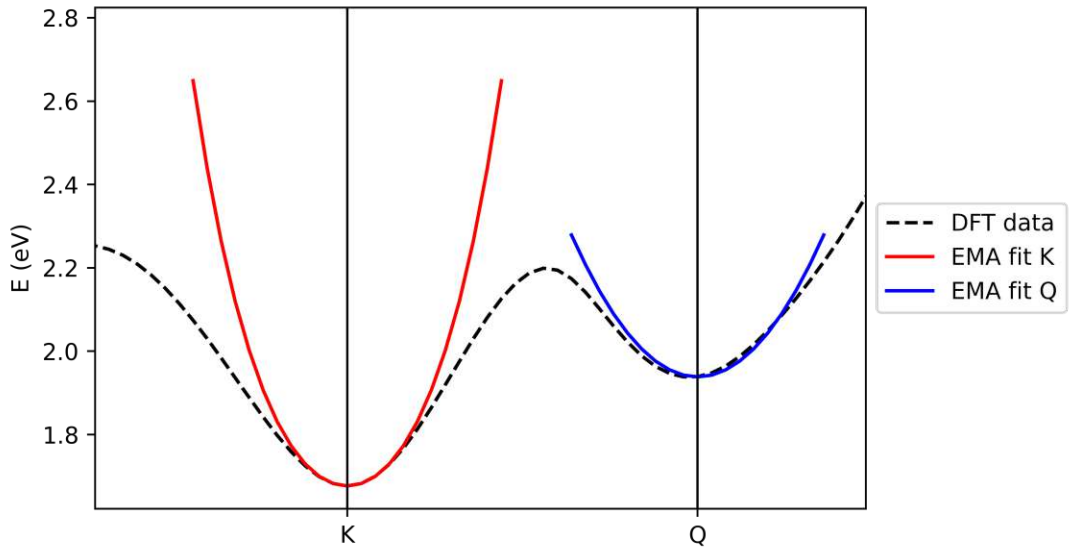
(a) Conduction band of monolayer MoS_2 with fit.
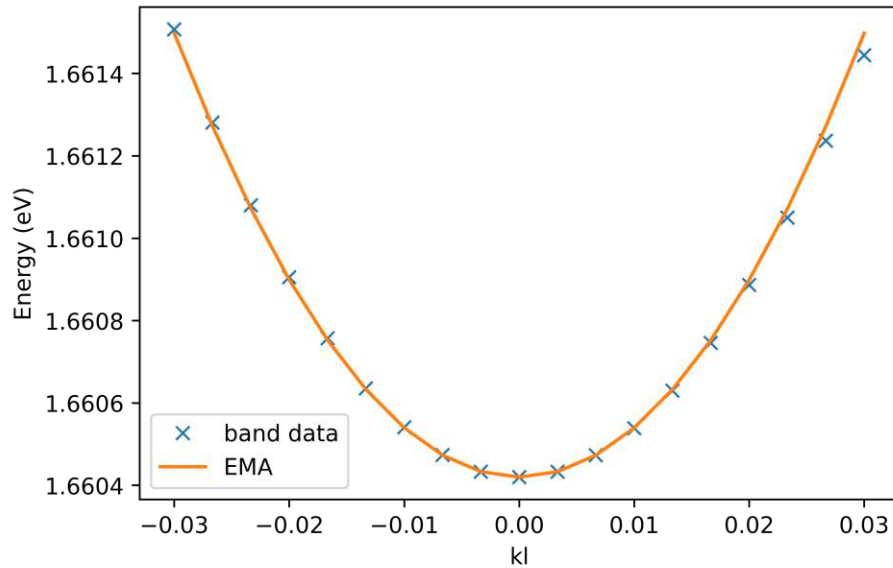
(b) Visualization of fit of the K-valley from (a).

Figure 4.15: Fitting for effective mass extraction for PBE without strain.

shape the effective masses are the same in both directions. Once again it can be observed, that the choice of pseudopotential has little influence, especially compared to the choice of functional, as once again all PBE calculations are grouped together. Even though the absolute values differ, a close to linear dependence of the change in the effective mass to strain can be seen. The slight deviations from linear behavior might be explained by numerical errors which occur when fitting close to the minima and the energy values become
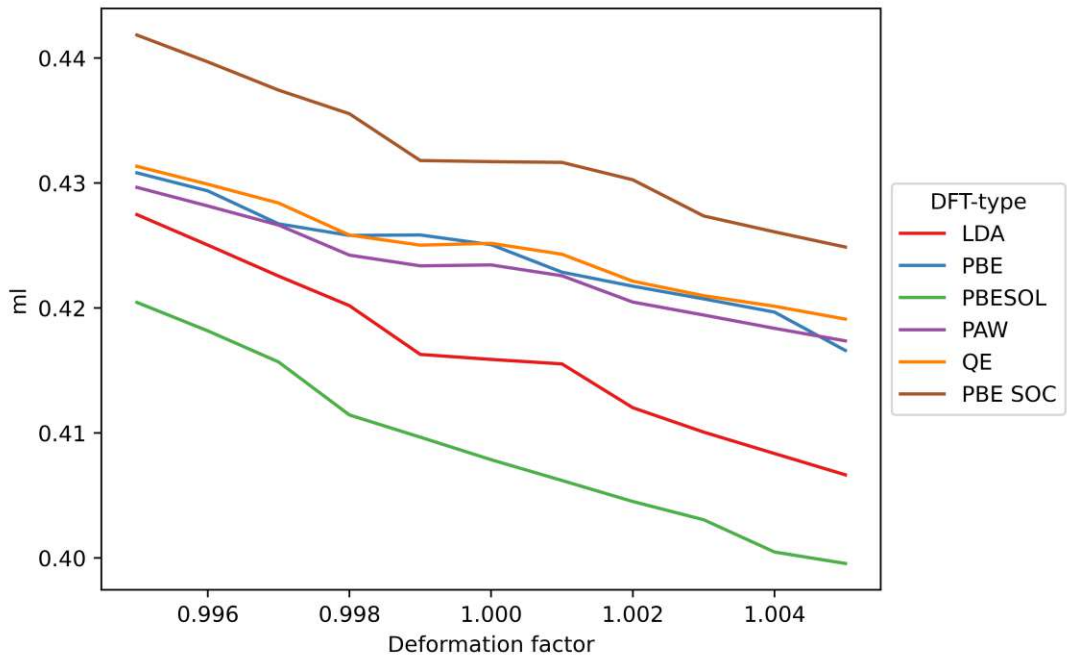
(a) Effective masses (ml, mt).
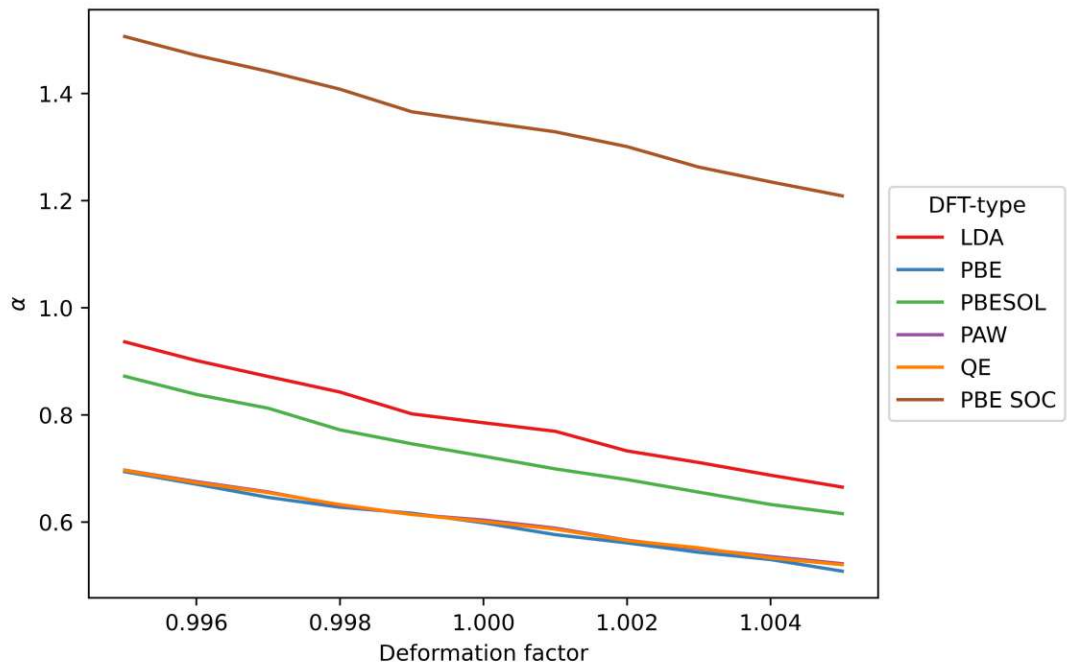
(b) Non-parabolicity factor α.

Figure 4.16: Influence of strain on the effective mass parameters for the K valley for different exchange-correlation functionals.

very small.

In Fig. 4.17 the effective masses for the Q valley and their dependence on the applied strain can be seen. As described for the K valley, all values resulting from PBE calculations are very similar; both longitudinal and transversal effective masses are much higher than those of other calculations. It is also interesting that the calculation with spin-orbit coupling shows the lowest longitudinal effective mass, but the highest transverse effective mass, which suggests a different shape of the Q valley compared to the other calculations. This is further supported when studying the non-parabolicity factor for the Q valley, as plotted in Fig. 4.18.

While the other DFT calculations show very little deviation from the parabolic form, the non-parabolicity factor of the PBE calculation including spin-orbit coupling is comparatively quite high. This further underlines the assumption that modeling the system in this manner could introduce a level of complexity which the model is simply not designed to accurately represent.

Finally, the results for the carrier mobility calculations are provided in Fig. 4.19.

The PBE calculations show a rather linear behavior with relatively high values of around 400 cm^2/(Vs). PBESOL shows a steep initial slope which changes into a more moderate slope. For LDA and PBE with spin-orbit coupling, the curve first seems exponential, then becomes somewhat linear between the deformation factors of 0.998 and 1.002, and then shows a similar behavior as the PBESOL curve by changing into a more moderate slope. These behavioral changes can be linked to certain calculated values of ΔE_{QK}. The change from exponential to linear takes place after surpassing an energy difference of around 0.05 eV, at the deformation factor 0.997 for PBE with SOC and 0.998 for LDA. The change from a steep slope to a more moderate slope takes place around 0.1 eV, which is at a deformation of 0.998 for PBESOL, 0.999 for PBE with SOC, and 1.002 for LDA. All PBE calculations have ΔE_{QK} values above that threshold value.

For the Ensemble Monte Carlo simulations, electrons are initialized with a certain energy distribution. In order for these electrons to scatter from the lower K valleys into the Q valleys they have to overcome this energy difference. Therefore, the higher the energy separation the more the energy onset of intervalley scattering increases. While for small, and even negative energy differences, scattering is very frequent and strongly limits the carrier mobility, its influence lessens for higher energy separation.

After a certain energy ΔE_{QK} becomes so large that the mobility is limited only by the intra- and intervalley scattering of the K valleys, as this is much more likely to take place. At this point, the slope of the curves becomes moderate. It also becomes clear that effective masses play a significant role. The valley energy separation, as can be seen in Fig 4.14, is fairly similar for PBE with spin-orbit coupling and LDA. Yet the resulting mobility-deformation curves are quite different, with LDA reaching much higher values. The effective mass parameters for both DFT calculation setups are quite different, see Fig. 4.16 and Fig. 4.17, especially for the K-valley and the transverse effective mass of the Q-valley.

Experimentally, a mobility of at least 200 cm^2/(Vs) has been reported for monolayer MoS$_2$
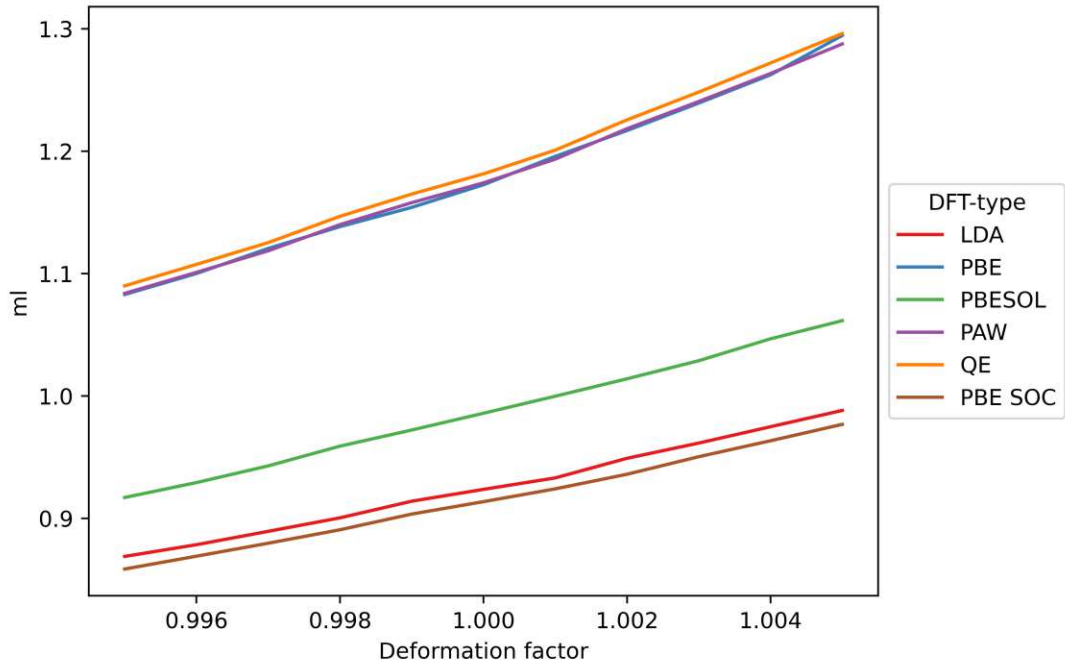
(a) Longitudinal effective mass ml.
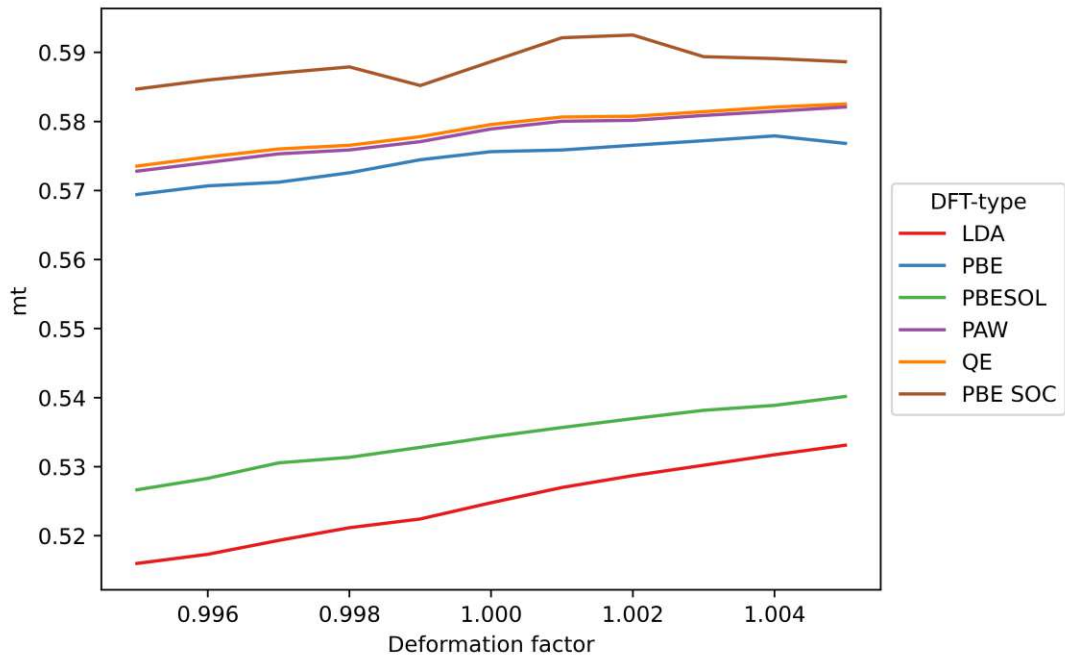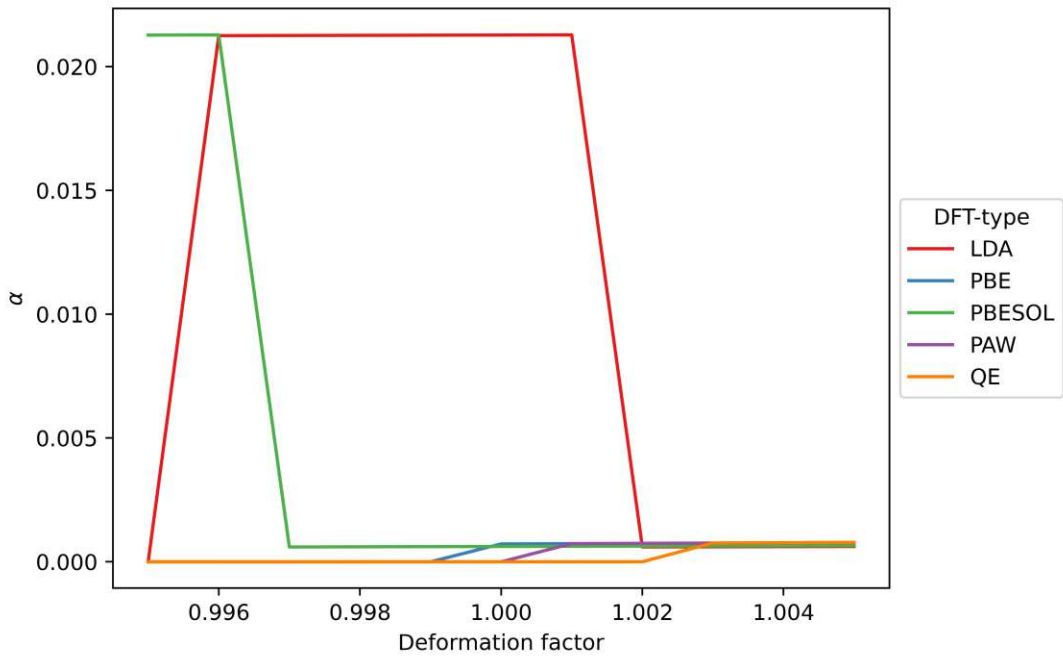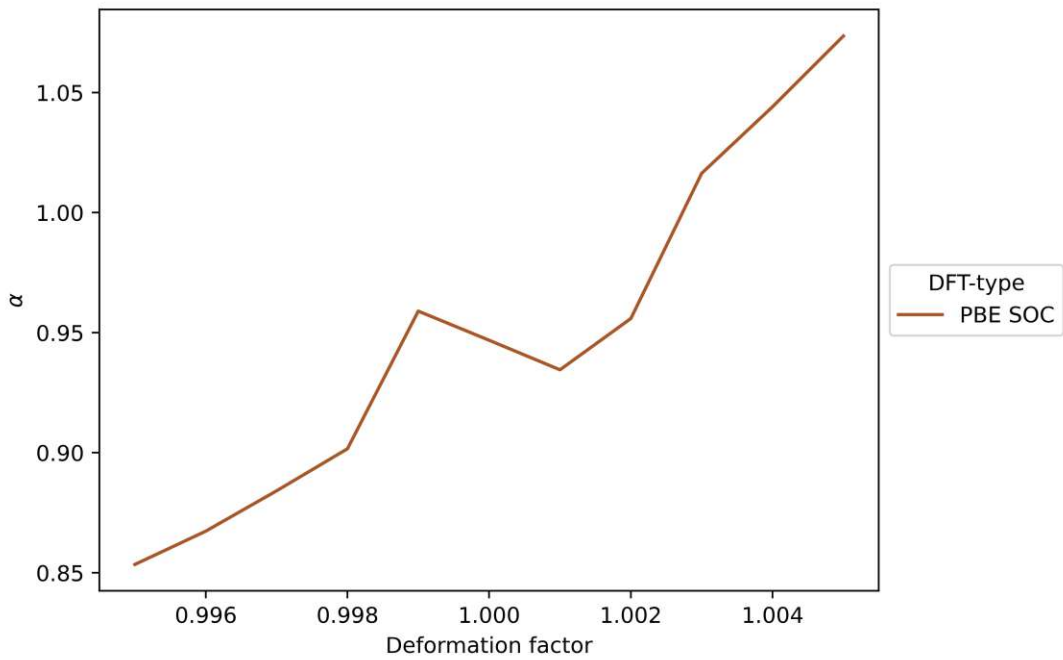

(b) Transverse effective mass mt.

Figure 4.17: Influence of strain on the effective mass parameters for the Q valley for different exchange-correlation functionals.

(a) Exchange-correlation functionals not including SOC

(b) PBE with SOC

Figure 4.18: Influence of strain on the non-parabolicity factor α for the Q valley for different exchange-correlation functionals.
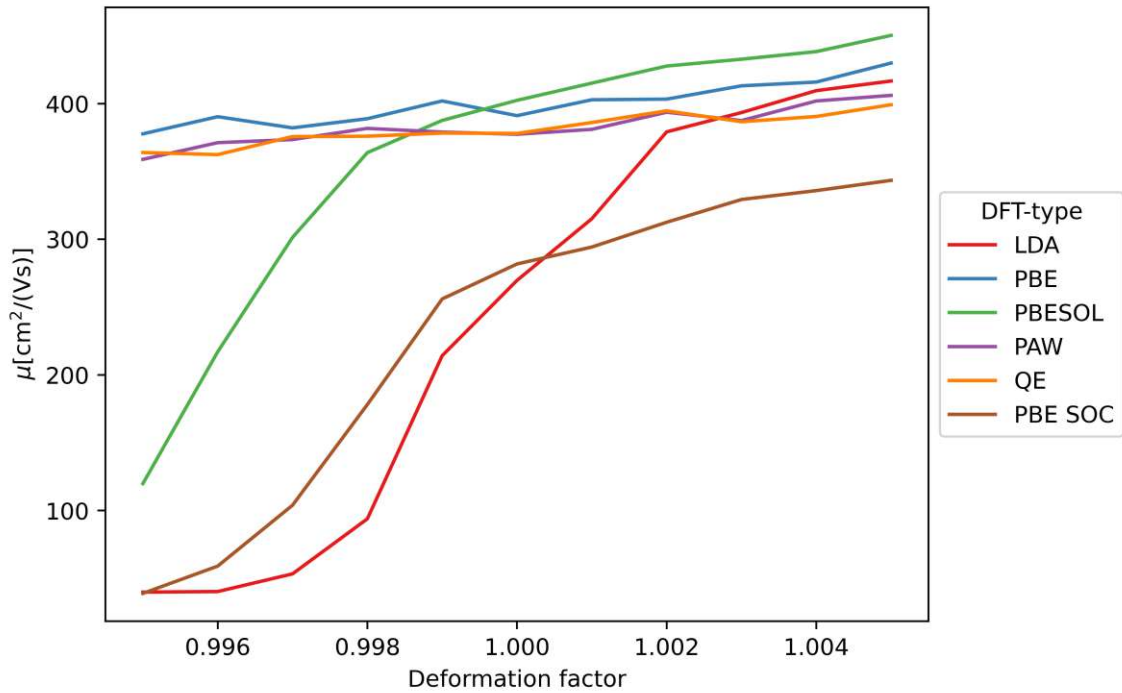
Figure 4.19: Influence of strain on the carrier mobility for all DFT-EMC calculations.

transistors [66]. This is a much lower value than the simulation results predict. It has to be noted that the model only includes inter- and intravalley scattering effects of Q and K valleys. In reality, many more factors influence the carrier mobility, and various scattering effects are being ignored. For example scattering due to crystal defects, impurities, other carriers, or interface scattering, especially surface scattering effects which play an important role in 2-D materials are not included here since we only study a suspended monolayer. Furthermore, there might be lattice scattering which exceeds those simulated in the EMC code. For real structures, the application of strain will likely disturb the symmetry allowing, for example, scattering between K-valleys of different energies or alterations of the deformation potential and therefore changing scatter rates.

As previously mentioned, only relatively small strains were investigated here. This choice was guided by two primary considerations. Firstly, for the calculations with LDA, the base assumption that the K valley is the lowest energy level of the conduction band did no longer hold for larger compressive strains. Secondly, in the case of PBE calculations separation values for ΔE_{QK} were quickly reached, after which the mobility no longer changed and most intervalley scattering ceased. An example of how the carrier mobility changes for larger strains of $\pm$ 5 %, the carrier mobility and ΔE_{QK} for PBE calculations is shown in Fig. 4.20.

For these larger deformations, PBE shows a similar range of mobilities as the LDA functional did for the smaller strains. Under a very strong compressive strain, the mobility
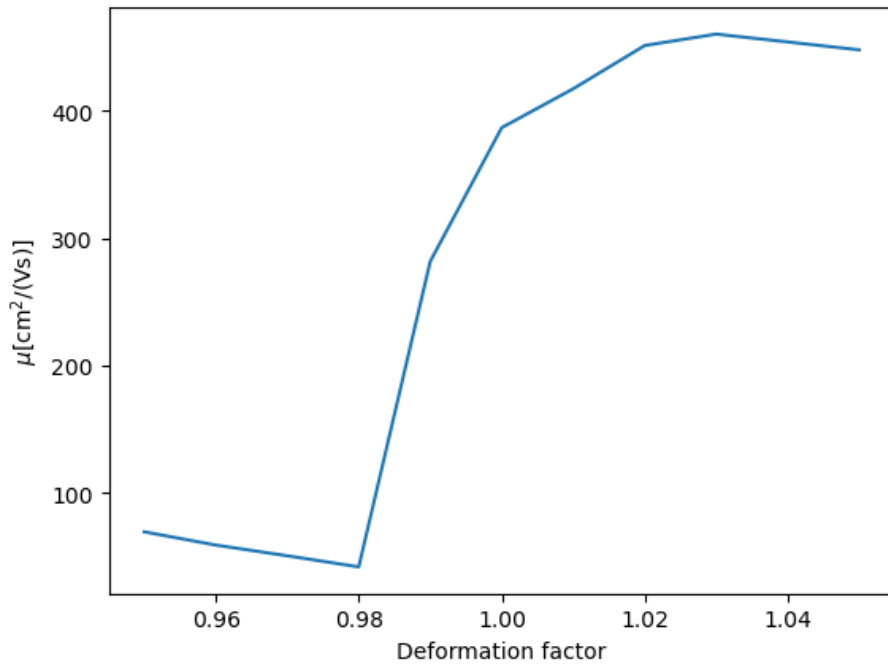
(a) Carrier mobility μ.
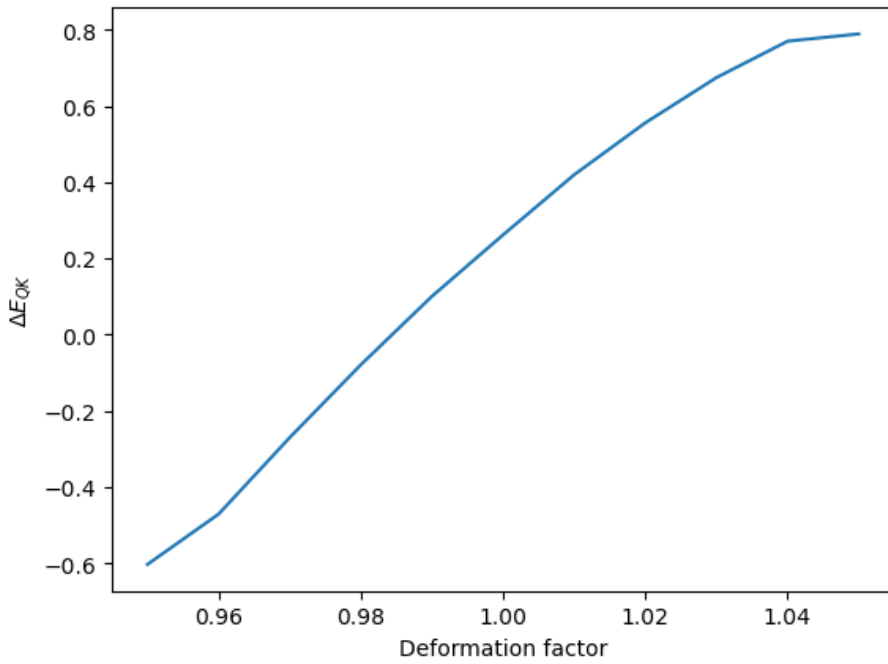
(b) Valley separation energy ΔE_{QK}.

Figure 4.20: Simulation results for PBE calculations and $\pm$ 5 % strains.

starts at about 70 cm^2/(Vs) and then decreases until it reaches a minimum of about 40 cm^2/(Vs) at a deformation factor of 0.98. When looking at the energy separation of the valleys it becomes clear that for strong compression the Q valley is lower than the K valley, leading to a decrease in scattering because now added energy is required for the electrons to scatter into the higher K valley. This energy difference decreases, as K slowly becomes the lower valley once again; this happens after a strain of about 2 % is applied, which is also when ΔE_{QK} is zero and no energy offset for inter valley scattering exists, leading to a minimum in mobility. After this point is reached, the change in ΔE_{QK} strongly influences the scattering and therefore the mobility until the curve starts to flatten around a mobility of 450 cm^2/(Vs).

As 2D materials have been promising for quite a while now, TMDs have been thoroughly investigated experimentally as well as theoretically. In this thesis, a strong dependence on how the *ab initio* study is set up was observed in the theoretical calculations. Despite this, it is important to note, that the same general trends can be seen for most DFT calculations made here. Within the investigated range of strains, the band gap increases for compressive strains and decreases for tensile strains. The opposite is true for the energy separation ΔE_{QK} between the minima of the Q and K valleys which decreases, and even becomes negative, for compressive strains and increases for tensile strains. The effective masses for the K valley become smaller with a larger deformation factor while those of the Q valley become larger. Finally, all DFT "flavors" showed that the mobility is reduced under compressive strain and increased under tensile strain.

For very strong compressive strains, the Q valley becomes lower than the K valley. In this case, ΔE_{QK} becomes negative, the intervalley scattering is limited by this energy difference, and the mobility is slightly increased. When moving closer to the equilibrium structure, ΔE_{QK} approaches zero; at this point the scattering rates are the highest and thus the mobility is at its lowest. After this phase, the ΔE_{QK} increases further, providing an energy barrier for scattering from the K valley into the now again higher Q valley. This increasing barrier gradually reduces the scatter rate, leading to higher mobilities. At a certain point, the separation energy becomes so significant that intervalley scattering is negligible and the mobility curve flattens. The effective masses and non-parabolicity factors of the different calculations play a role insofar as lower effective masses correlate with higher mobilities; this can be observed especially for tensile strain, where the mobility is determined by intravalley scattering in the K-valley. The K effective masses are the lowest for PBESOL, it reaches the highest mobility values. While LDA and PBE with SOC have very similar values for ΔE_{QK}, PBE with SOC has the highest effective masses for the K valley and therefore also lower mobility values, even when comparing strains at which they have a similar energy separation.

To fully judge whether the inclusion of spin-orbit coupling is beneficial and adds to the accuracy of the simulation, the model would first need to be adjusted to include spin effects and to allow for a more complex approximation of the band structure. This is beyond the scope of this work, but it can be assumed that in this chain of assumptions and models, from *ab initio* DFT calculations to applying the Monte Carlo method to solve the Boltzmann Transport Equation, the result is only as accurate as the weakest approximation.

Therefore, even if spin-orbit coupling were to yield perfect results, it would represent an unnecessary effort within the constraints of our current model, as they cannot be effectively integrated to improve the final outcomes.

Finally, it was shown that the carrier mobility in monolayer MoS_2 changes when strain is applied. Furthermore, there exists a strain interval for which this dependence is linear. Where this interval lies is different for each "flavor" of DFT calculations. Therefore, in order to effectively use this phenomenon for the development of a stain-based sensor, it is necessary to establish a robust calibration procedure.

5 Conclusion

In studying the metal-organic frameworks, this thesis primarily focused on structure optimizations, although this was not the initial main goal. The aim was to come up with a practical method for calculating these structures to ultimately study surface properties, and predict MOF-analyte interactions. The selected *ab initio* approach proved challenging in terms of computational cost, and convergence behavior. MOFs pose a challenge in simulations due to their large structures with a wide variety of bonds and interaction types. These include complex bonds between linkers and ions, covalent bonds within organic linkers, long-range Van der Waals interactions, and hydrogen bonds. Accurately describing all of these interactions can be exceptionally demanding for DFT calculations, often requiring special modifications which significantly increase computational efforts. Therefore, seeking the optimal structure through this approach may not be the most reasonable course of action.

A better approach might involve relying on experimental methods, such as X-ray absorption spectroscopy or X-ray diffraction, to obtain more detailed information about the MOF's structure. Alternatively, one could explore computationally efficient prediction methods, such as machine learning based approaches. An empirically backed structure derived from such methods could serve as a robust foundation for further investigations into the potential of the MOF as an analyte sensor.

The influence of strain on the carrier mobility in monolayer MoS_2 was investigated theoretically. For this purpose Density Functional Theory calculations with different exchange-correlation functionals and pseudopotentials were performed; additionally, calculations including spin-orbit coupling were executed. The *ab initio* methods were used to investigate the electronic structure of the MoS_2 film, and a fitting process served to determine critical parameters in order to approximate the conduction band. These factors include the effective masses, non-parabolicity factors, and the energy difference ΔE_{QK} between them, which characterize the K and Q valleys. These parameters served as inputs in the Ensemble Monte Carlo simulations, which were applied to solve the Boltzmann Transport Equation in order to calculate the carrier mobility. The simulations accounted for intra- and inter-valley scattering effects caused by optical and acoustic phonons. The results show that tensile strain enhances carrier mobility, whereas compressive strain decreases it. The mobility is notably influenced by the energy separation between these valleys, which strongly depends on the choice of exchange-correlation functional employed in the DFT calculations.

It was not possible to conclude whether taking spin-orbit coupling into account added a benefit to the model accuracy, neither could a favorable DFT setup be established. As expected, the choice of pseudopotentials or the use of PAW only has a marginal influence

on the results of the calculations. Independent of the functional used, linear regions were found for the mobility-strain curve, which shows promise for strain engineering of MoS_2 layers or its application as a stress sensor.

Computational methods and approaches must be chosen wisely and many considerations have to be made: What property needs to be investigated? Is the user interested in the electronic structure in the ground state, in its exited states, band gaps, vibrational modes, transition states, geometry, or magnetic moments? What special properties of the material might pose restrictions or have to be accounted for in the model explicitly? Can a significant impact of van der Waals forces be expected, like in multilayer MoS_2 or between the linkers of metal-organic frameworks? Is the material conducting or semiconducting, can a specific magnetic behavior be expected? For each additional complexity which is added to DFT calculations, one also must be aware that there is a price to pay in computing time.

Fundamentally, it has been demonstrated that Density Functional Theory (DFT) serves as a valuable tool for calculating relevant material properties. It was possible to investigate the strain dependence of the carrier mobility of 2D MoS_2 based on *ab initio* calculations. As a method, DFT has the potential to optimize the use of resources by doing an initial screening of multiple candidate materials. Further, DFT complements the empirical approach by assisting the theoretical analysis of experimental outcomes. Nevertheless, it is also necessary to acknowledge the limitations of the method, as the chosen approach for investigating the MOF structures proved to be overly resource-intensive and impractical.

Finally, the indispensable role of experimental validation must be mentioned. Combining computational and experimental, as well as theoretical and practical, research, is the most effective means for advancing scientific knowledge.

Bibliography

[1] X. Fang, B. Zong, and S. Mao, „Metal–organic framework-based sensors for environmental contaminant sensing", *Nano-micro letters*, vol. 10, pp. 1–19, 2018. DOI: `10.1007/s40820-018-0218-0`.

[2] Y. Dai, T. Xue, X. Han, *et al.*, „Suspended 2d materials: A short review", *Crystals*, vol. 13, no. 9, p. 1337, 2023. DOI: `10.3390/cryst13091337`.

[3] D. J. Collins and H.-C. Zhou, „Hydrogen storage in metal-organic frameworks", *Journal of materials chemistry*, vol. 17, no. 30, pp. 3154–3160, 2007. DOI: `10.1039/b702858j`.

[4] J.-R. Li, R. J. Kuppler, and H.-C. Zhou, „Selective gas adsorption and separation in metal-organic frameworks", *Chemical Society Reviews*, vol. 38, no. 5, pp. 1477–1504, 2009. DOI: `10.1039/b802426j`.

[5] J. Lee, O. K. Farha, J. Roberts, K. A. Scheidt, S. T. Nguyen, and J. T. Hupp, „Metal–organic framework materials as catalysts", *Chemical Society Reviews*, vol. 38, no. 5, pp. 1450–1459, 2009. DOI: `10.1039/b807080f`.

[6] L. E. Kreno, K. Leong, O. K. Farha, M. Allendorf, R. P. Van Duyne, and J. T. Hupp, „Metal–organic framework materials as chemical sensors", *Chemical reviews*, vol. 112, no. 2, pp. 1105–1125, 2012. DOI: `10.1021/cr200324t`.

[7] H. Furukawa, K. E. Cordova, M. O'Keeffe, and O. M. Yaghi, „The chemistry and applications of metal-organic frameworks", *Science*, vol. 341, no. 6149, p. 1 230 444, 2013. DOI: `10.1126/science.1230444`.

[8] H. Deng, S. Grunder, K. E. Cordova, *et al.*, „Large-pore apertures in a series of metal-organic frameworks", *science*, vol. 336, no. 6084, pp. 1018–1023, 2012. DOI: `10.1126/science.1220131`.

[9] W. Liang, P. Wied, F. Carraro, *et al.*, „Metal–organic framework-based enzyme biocomposites", *Chemical Reviews*, vol. 121, no. 3, pp. 1077–1129, 2021. DOI: `10.1021/acs.chemrev.0c01029`.

[10] N. C. Burtch, H. Jasuja, and K. S. Walton, „Water stability and adsorption in metal–organic frameworks", *Chemical reviews*, vol. 114, no. 20, pp. 10 575–10 612, 2014. DOI: `10.1021/cr5002589`.

[11] K. W. Chapman, G. J. Halder, and P. J. Chupas, „Pressure-induced amorphization and porosity modification in a metal-organic framework", *Journal of the American Chemical Society*, vol. 131, no. 48, pp. 17 546–17 547, 2009. DOI: `10.1021/ja908415z`.

[12] S. Grimme, „Density functional theory with London dispersion corrections", *Wiley Interdisciplinary Reviews: Computational Molecular Science*, vol. 1, no. 2, pp. 211–228, 2011. DOI: `10.1002/wcms.30`.

[13] J. L. Mancuso, A. M. Mroz, K. N. Le, and C. H. Hendon, „Electronic structure modeling of metal–organic frameworks", *Chemical reviews*, vol. 120, no. 16, pp. 8641–8715, 2020. DOI: 10.1021/acs.chemrev.0c00148.

[14] H. Xu, F. Liu, Y. Cui, B. Chen, and G. Qian, „A luminescent nanoscale metal–organic framework for sensing of nitroaromatic explosives", *Chemical Communications*, vol. 47, no. 11, pp. 3153–3155, 2011. DOI: 10.1039/c0cc05166g.

[15] Y. Cui, F. Zhu, B. Chen, and G. Qian, „Metal–organic frameworks for luminescence thermometry", *Chemical Communications*, vol. 51, no. 35, pp. 7420–7431, 2015. DOI: 10.1039/c5cc00718f.

[16] J. Chang, X. Wang, J. Wang, H. Li, and F. Li, „Nucleic acid-functionalized metal–organic framework-based homogeneous electrochemical biosensor for simultaneous detection of multiple tumor biomarkers", *Analytical chemistry*, vol. 91, no. 5, pp. 3604–3610, 2019. DOI: 10.1021/acs.analchem.8b05599.

[17] E.-X. Chen, H. Yang, and J. Zhang, „Zeolitic imidazolate framework as formaldehyde gas sensor", *Inorganic chemistry*, vol. 53, no. 11, pp. 5411–5413, 2014. DOI: 10.1021/ic500474j.

[18] J. Aguilera-Sigalat and D. Bradshaw, „A colloidal water-stable MOF as a broad-range fluorescent pH sensor via post-synthetic modification", *Chemical Communications*, vol. 50, no. 36, pp. 4711–4713, 2014. DOI: 10.1039/c4cc00659c.

[19] R. Zhang, W. Song, M. Wang, and H. Ji, „Controlling the size of a Zn-MOF through ligand exchange and pore-tailored ZnO assemblies for size-selective gas sensing", *CrystEngComm*, vol. 21, no. 42, pp. 6414–6422, 2019. DOI: 10.1039/C9CE01184F.

[20] J. Sun, X. Li, W. Guo, *et al.*, „Synthesis methods of two-dimensional MoS_2: A brief review", *Crystals*, vol. 7, no. 7, p. 198, 2017. DOI: 10.3390/cryst7070198.

[21] A. Splendiani, L. Sun, Y. Zhang, *et al.*, „Emerging photoluminescence in monolayer MoS_2", *Nano letters*, vol. 10, no. 4, pp. 1271–1275, 2010. DOI: 10.1021/nl903868w.

[22] A. Kokalj, „XCrySDen—a new program for displaying crystalline structures and electron densities", *Journal of Molecular Graphics and Modelling*, vol. 17, no. 3-4, pp. 176–179, 1999. DOI: 10.1016/s1093-3263(99)00028-5.

[23] X. Wang, W. Xing, X. Feng, L. Song, and Y. Hu, „MoS_2/polymer nanocomposites: preparation, properties, and applications", *Polymer Reviews*, vol. 57, no. 3, pp. 440–466, 2017. DOI: 10.1080/15583724.2017.1309662.

[24] F. K. Perkins, A. L. Friedman, E. Cobas, P. Campbell, G. Jernigan, and B. T. Jonker, „Chemical vapor sensing with monolayer MoS_2", *Nano letters*, vol. 13, no. 2, pp. 668–673, 2013. DOI: 10.1021/nl3043079.

[25] A. Shokri and N. Salami, „Gas sensor based on MoS_2 monolayer", *Sensors and Actuators B: Chemical*, vol. 236, pp. 378–385, 2016. DOI: 10.1016/j.snb.2016.06.033.

[26] D. Ma, W. Ju, T. Li, *et al.*, „The adsorption of CO and NO on the MoS_2 monolayer doped with Au, Pt, Pd, or Ni: A first-principles study", *Applied Surface Science*, vol. 383, pp. 98–105, 2016. DOI: 10.1016/j.apsusc.2016.04.171.

[27] T. E. Gber, H. Louis, A. E. Owen, *et al.*, „Heteroatoms (Si, B, N, and P) doped 2D monolayer MoS 2 for NH 3 gas detection", *RSC advances*, vol. 12, no. 40, pp. 25 992–26 010, 2022. DOI: 10.1039/D2RA04028J.

[28] S. Demers, *Advanced density functional theory methods for materials science*. California Institute of Technology, 2014.

[29] P. Hohenberg and W. Kohn, „Inhomogeneous electron gas“, *Physical review*, vol. 136, no. 3B, B864, 1964. DOI: `10.1103/physrev.136.b864`.

[30] W. Kohn and L. J. Sham, „Self-consistent equations including exchange and correlation effects“, *Physical review*, vol. 140, no. 4A, A1133, 1965. DOI: `10.1103/physrev.140.a1133`.

[31] D. M. Ceperley and B. J. Alder, „Ground state of the electron gas by a stochastic method“, *Physical review letters*, vol. 45, no. 7, p. 566, 1980. DOI: `10.2172/5208790`.

[32] J. P. Perdew, K. Burke, and M. Ernzerhof, „Generalized gradient approximation made simple“, *Physical review letters*, vol. 77, no. 18, p. 3865, 1996. DOI: `10.1103/physrevlett.77.3865`.

[33] J. P. Perdew, A. Ruzsinszky, G. I. Csonka, *et al.*, „Restoring the density-gradient expansion for exchange in solids and surfaces“, *Physical review letters*, vol. 100, no. 13, p. 136 406, 2008. DOI: `10.1103/physrevlett.100.136406`.

[34] R. M. Martin, *Electronic structure: basic theory and practical methods.* Cambridge university press, 2020. DOI: `10.1017/9781108555586`.

[35] D. Hamann, M. Schlüter, and C. Chiang, „Norm-conserving pseudopotentials“, *Physical Review Letters*, vol. 43, no. 20, p. 1494, 1979. DOI: `10.1103/physrevlett.43.1494`.

[36] D. Vanderbilt, „Soft self-consistent pseudopotentials in a generalized eigenvalue formalism“, *Physical review B*, vol. 41, no. 11, p. 7892, 1990. DOI: `10.1103/physrevb.41.7892`.

[37] V. Galitski and I. B. Spielman, „Spin–orbit coupling in quantum gases“, *Nature*, vol. 494, no. 7435, pp. 49–54, 2013. DOI: `10.1038/nature11841`.

[38] P. Giannozzi, S. Baroni, N. Bonini, *et al.*, „QUANTUM ESPRESSO: a modular and open-source software project for quantum simulations of materials“, *Journal of physics: Condensed matter*, vol. 21, no. 39, p. 395 502, 2009. DOI: `10.1088/0953-8984/21/39/395502`.

[39] P. Giannozzi, O. Andreussi, T. Brumme, *et al.*, „Advanced capabilities for materials modelling with Quantum ESPRESSO“, *Journal of physics: Condensed matter*, vol. 29, no. 46, p. 465 901, 2017. DOI: `10.1088/1361-648x/aa8f79`.

[40] A. Pilotto, P. Khakbaz, P. Palestri, and D. Esseni, „Semi-classical transport in MoS_2 and MoS_2 transistors by a Monte Carlo approach“, *Solid-State Electronics*, vol. 192, p. 108 295, 2022, ISSN: 0038-1101. DOI: `https://doi.org/10.1016/j.sse.2022.108295`. [Online]. Available: `https://www.sciencedirect.com/science/article/pii/S0038110122000673`.

[41] M. El-Saba, „Semiclassical transport theory of charge carriers, part i: Microscopic approaches“, in *Transport of Information-Carriers in Semiconductors and Nanodevices*, IGI Global, 2017, pp. 72–137. DOI: `10.4018/978-1-5225-2312-3.ch002`.

[42] L. Gollner, R. Steiner, A. Benzer, and L. Filipovic. „ViennaEMC“. (2023), [Online]. Available: `https://github.com/ViennaTools/ViennaEMC/` (visited on 07/20/2023).

[43] Z. Stanojević, „Physical mobility modeling for TCAD device simulation“, Ph.D. dissertation, Vienna University of Technology, 2016. DOI: `10.34726/hss.2016.37966`.

[44] D. K. Ferry, *Semiconductor Transport.* Taylor & Francis, 2000, ISBN 978-0-748-40866-5. DOI: `10.1201/b21468`.

[45] S. S. Li, *Semiconductor physical electronics.* Springer Science & Business Media, 2012.

[46] X. Li, J. T. Mullen, Z. Jin, K. M. Borysenko, M. B. Nardelli, and K. W. Kim, „Intrinsic electrical transport properties of monolayer silicene and MoS_2 from first principles", *Physical Review B*, vol. 87, no. 11, p. 115 418, 2013. DOI: `10.1103/PhysRevB.87.115418`.

[47] L. Gollner, „Development and Application of an Ensemble Monte Carlo Framework", Master's thesis, Vienna University of Technology, 2023. DOI: `10.34726/hss.2023.95902`.

[48] C. Jacoboni and P. Lugli, *The Monte Carlo Method for Semiconductor Device Simulation*. Springer Science Business Media, 2012, ISBN 978-3-709-16963-6.

[49] S. Zhao, Y. Wang, J. Dong, *et al.*, „Ultrathin metal–organic framework nanosheets for electrocatalytic oxygen evolution", *Nature Energy*, vol. 1, no. 12, pp. 1–10, 2016. DOI: `10.1038/nenergy.2016.184`.

[50] A. Jain, S. P. Ong, G. Hautier, *et al.*, „Commentary: The Materials Project: A materials genome approach to accelerating materials innovation", *APL materials*, vol. 1, no. 1, 2013. DOI: `10.1063/1.4812323`.

[51] A. S. Rosen, S. M. Iyer, D. Ray, *et al.*, „Machine learning the quantum-chemical properties of metal–organic frameworks for accelerated materials discovery", *Matter*, vol. 4, no. 5, pp. 1578–1597, 2021. DOI: `10.1016/j.matt.2021.02.015`.

[52] A. S. Rosen, V. Fung, P. Huck, *et al.*, „High-throughput predictions of metal–organic framework electronic properties: theoretical challenges, graph neural networks, and data exploration", *npj Computational Materials*, vol. 8, no. 1, p. 112, 2022. DOI: `10.1038/s41524-022-00796-6`.

[53] K. Momma and F. Izumi, „VESTA 3 for three-dimensional visualization of crystal, volumetric and morphology data", *Journal of applied crystallography*, vol. 44, no. 6, pp. 1272–1276, 2011. DOI: `10.1107/S0021889811038970`.

[54] T. D. Kühne, M. Iannuzzi, M. Del Ben, *et al.*, „CP2K: An electronic structure and molecular dynamics software package-Quickstep: Efficient and accurate electronic structure calculations", *The Journal of Chemical Physics*, vol. 152, no. 19, 2020. DOI: `10.1063/5.0007045`.

[55] C. Adamo and V. Barone, „Toward reliable density functional methods without adjustable parameters: The PBE0 model", *The Journal of chemical physics*, vol. 110, no. 13, pp. 6158–6170, 1999. DOI: `10.1063/1.478522`.

[56] „How to Converge the CUTOFF and REL_CUTOFF". (2020), [Online]. Available: `https://www.cp2k.org/howto:converging_cutoff` (visited on 08/25/2023).

[57] D. Hamann, „Optimized norm-conserving Vanderbilt pseudopotentials", *Physical Review B*, vol. 88, no. 8, p. 085 117, 2013. DOI: `10.1103/physrevb.88.085117`.

[58] „Quantum Espresso Pseudopotentials Library". (2019), [Online]. Available: `https://pseudopotentials.quantum-espresso.org/legacy_tables` (visited on 08/08/2023).

[59] S. A. Tawfik, O. Isayev, C. Stampfl, J. Shapter, D. A. Winkler, and M. J. Ford, „Efficient prediction of structural and electronic properties of hybrid 2d materials using complementary dft and machine learning approaches", *Advanced Theory and Simulations*, vol. 2, no. 1, p. 1 800 128, 2019. DOI: `10.1002/adts.201800128`.

[60] C. R. Harris, K. J. Millman, S. J. Van Der Walt, *et al.*, „Array programming with NumPy", *Nature*, vol. 585, no. 7825, pp. 357–362, 2020. DOI: `10.1038/s41586-020-2649-2`.

[61] K. Berland, V. R. Cooper, K. Lee, *et al.*, „Van der waals forces in density functional theory: A review of the vdw-df method", *Reports on Progress in Physics*, vol. 78, no. 6, p. 066 501, 2015. DOI: `10.1088/0034-4885/78/6/066501`.

[62] M. Guidon, J. Hutter, and J. VandeVondele, „Auxiliary density matrix methods for Hartree- Fock exchange calculations", *Journal of chemical theory and computation*, vol. 6, no. 8, pp. 2348–2364, 2010. DOI: `10.1021/ct1002225`.

[63] A. Al-Hilli and B. Evans, „The preparation and properties of transition metal dichalcogenide single crystals", *Journal of Crystal Growth*, vol. 15, no. 2, pp. 93–101, 1972. DOI: `10.1016/0022-0248(72)90129-7`.

[64] V. Petkov, S. Billinge, P. Larson, *et al.*, „Structure of nanocrystalline materials using atomic pair distribution function analysis: Study of LiMoS 2", *Physical Review B*, vol. 65, no. 9, p. 092 105, 2002. DOI: `10.1103/PhysRevB.65.092105`.

[65] S. Deng, L. Li, and M. Li, „Stability of direct band gap under mechanical strains for monolayer MoS_2, $MoSe_2$, WS_2 and WSe_2", *Physica E: Low-dimensional Systems and Nanostructures*, vol. 101, pp. 44–49, 2018. DOI: `10.1016/j.physe.2018.03.016`.

[66] B. Radisavljevic, A. Radenovic, J. Brivio, V. Giacometti, and A. Kis, „Single-layer MoS_2 transistors", *Nature nanotechnology*, vol. 6, no. 3, pp. 147–150, 2011. DOI: `10.1038/nnano.2010.279`.